KTH Engineering Sciences

Spectral Mammography with X-Ray Optics and a Photon-Counting Detector

ERIK FREDENBERG

Doctoral Thesis
Stockholm, Sweden 2009

TRITA-FYS 2009:69
ISSN 0280-316X
ISRN KTH/FYS/--09:69--SE
ISBN 978-91-7415-516-7

KTH Fysik
SE-106 91 Stockholm
SWEDEN

Akademisk avhandling som med tillstånd av Kungliga Tekniska Högskolan framlägges till offentlig granskning för avläggande av teknologie doktorsexamen i fysik fredagen den 18 december 2009 klockan 10.00 i Kollegiesalen, Lindstedtsvägen 26, Kungliga Tekniska Högskolan, Stockholm.
Fakultetsopponent: Associate Professor Jeffrey H. Siewerdsen.
Betygsnämnd: Docent Magnus Båth, Med Dr. Bedrich Vitak, Docent Ulrich Vogt.

© Erik Fredenberg, december 2009

Tryck: Universitetsservice US AB, typsatt i LaTeX

Abstract

Early detection is vital to successfully treating breast cancer, and mammography screening is the most efficient and wide-spread method to reach this goal. Imaging low-contrast targets, while minimizing the radiation exposure to a large population is, however, a major challenge. Optimizing the image quality per unit radiation dose is therefore essential. In this thesis, two optimization schemes with respect to x-ray photon energy have been investigated: filtering the incident spectrum with refractive x-ray optics (spectral shaping), and utilizing the transmitted spectrum with energy-resolved photon-counting detectors (spectral imaging).

Two types of x-ray lenses were experimentally characterized, and modeled using ray tracing, field propagation, and geometrical optics. Spectral shaping reduced dose approximately 20% compared to an absorption-filtered reference system with the same signal-to-noise ratio, scan time, and spatial resolution. In addition, a focusing pre-object collimator based on the same type of optics reduced divergence of the radiation and improved photon economy by about 50%.

A photon-counting silicon detector was investigated in terms of energy resolution and its feasibility for spectral imaging. Contrast-enhanced tumor imaging with a system based on the detector was characterized and optimized with a model that took anatomical noise into account. Improvement in an ideal-observer detectability index by a factor of 2 to 8 over that obtained by conventional absorption imaging was found for different levels of anatomical noise and breast density. Increased conspicuity was confirmed by experiment. Further, the model was extended to include imaging of unenhanced lesions. Detectability of microcalcifications increased no more than a few percent, whereas the ability to detect large tumors might improve on the order of 50% despite the low attenuation difference between glandular and cancerous tissue. It is clear that inclusion of anatomical noise and imaging task in spectral optimization may yield completely different results than an analysis based solely on quantum noise.

Key words: mammography; x-ray optics; photon counting; spectral shaping; spectral imaging; collimation; radiation dose; signal-to-noise ratio; quantum noise; anatomical noise; spatial resolution; x-ray flux;

Till Jennie och Hannes.

Publications

This thesis is based on the following papers, which will be referred to by their Roman numerals.

I. E. Fredenberg, B. Cederström, M. Åslund, C. Ribbing, and M. Danielsson. A tunable energy filter for medical x-ray imaging. *X-Ray Optics and Instrumentation*, 2008(635024):8 pages, 2008.

II. E. Fredenberg, B. Cederström, M. Åslund, P. Nillius, and M. Danielsson. An efficient pre-object collimator based on an x-ray lens. *Medical Physics*, 36(2): 626–633, 2009.

III. E. Fredenberg, B. Cederström, P. Nillius, C. Ribbing, S. Karlsson, and M. Danielsson. A low-absorption x-ray energy filter for small-scale applications. *Optics Express*, 17(14):11388–11398, 2009.

IV. E. Fredenberg, B. Cederström, and M. Danielsson. Energy filtering with x-ray lenses: Optimization for photon-counting mammography. *Radiation Protection Dosimetry*, 2009. Submitted for publication.

V. E. Fredenberg, M. Lundqvist, B. Cederström, M. Åslund, and M. Danielsson. Energy resolution of a photon-counting silicon strip detector. *Nuclear Instruments and Methods in Physics Research Section A*, 2009. Accepted for publication.

VI. E. Fredenberg, M. Hemmendorff, B. Cederström, M. Åslund, and M. Danielsson. Contrast-enhanced spectral mammography with a photon-counting detector. *Medical Physics*, 2009. Submitted for publication.

Reprints were made with permission from the publishers.

The author has contributed to the following publications, which are to some extent related to the thesis but not included.

- M. Åslund, E. Fredenberg, B. Cederström, and M. Danielsson. Spectral shaping for photon counting digital mammography. *Nucl. Instr. and Meth. A*, 580(2):1046–1049, 2007.
- E. Fredenberg, B. Cederström, C. Ribbing, and M. Danielsson. Prism-array lenses for energy filtering in medical x-ray imaging. In M. J. Flynn and J. Hsieh, editors, *Proc. SPIE, Physics of Medical Imaging*, volume 6510, 2007.
- E. Fredenberg, B. Cederström, M. Åslund, P. Nillius, M. Lundqvist, and M. Danielsson. Imaging with multi-prism x-ray lenses. In J. Hsieh and E. Samei, editors, *Proc. SPIE, Physics of Medical Imaging*, volume 6913, 2008.
- E. Fredenberg, B. Cederström, M. Lundqvist, C. Ribbing, M. Åslund, F. Diekmann, R. Nishikawa, and M. Danielsson. Contrast-enhanced dual-energy subtraction imaging using electronic spectrum-splitting and multi-prism x-ray lenses. In J. Hsieh and E. Samei, editors, *Proc. SPIE, Physics of Medical Imaging*, volume 6913, 2008.
- E. Fredenberg, M. Lundqvist, M. Åslund, M. Hemmendorff, B. Cederström, and M. Danielsson. A photon-counting detector for dual-energy breast tomosynthesis. In J. Hsieh and E. Samei, editors, *Proc. SPIE, Physics of Medical Imaging*, volume 7258, 2009.
- L. del Risco Norrlid, E. Fredenberg, M. Hemmendorff, C. Jackowski, and M. Danielsson. Imaging of small children with a prototype for photon counting tomosynthesis. In J. Hsieh and E. Samei, editors, *Proc. SPIE, Physics of Medical Imaging*, volume 7258, 2009.
- M. Yveborg, C. Xu, E. Fredenberg, and M. Danielsson. Photon-counting CT with silicon detectors: feasibility for pediatric imaging. In J. Hsieh and E. Samei, editors, *Proc. SPIE, Physics of Medical Imaging*, volume 7258, 2009.
- M. Åslund, E. Fredenberg, M. Telman, and M. Danielsson. Detectors for the future of x-ray imaging. *Radiat. Prot. Dosimetry*, 2009. Submitted for publication.

Contents

Publications **vii**

Contents **ix**

1 Introduction **1**
- 1.1 Breast Cancer and Mammography Screening 1
- 1.2 Digital Mammography 2
  - 1.2.1 From film, over energy integration, to photon counting 2
  - 1.2.2 Photon-counting detectors in a multi-slit geometry 3
  - 1.2.3 Beam focusing with x-ray optics 3
- 1.3 The X-Ray Energy Spectrum 4
  - 1.3.1 Spectral shaping with x-ray optics 5
  - 1.3.2 Spectral imaging with a photon-counting detector 6
- 1.4 Outline of the Thesis and Connection to Previous Work 7
- 1.5 Author's Contribution 8

2 X-Ray Optics **9**
- 2.1 Materials and Methods 9
  - 2.1.1 Background 9
  - 2.1.2 Spectral shaping 11
  - 2.1.3 Beam focusing 17
- 2.2 Results and Discussion 17
  - 2.2.1 Spectral shaping 17
  - 2.2.2 Beam focusing 22

3 Spectral Imaging **25**
- 3.1 Materials and Methods 25
  - 3.1.1 Background 25
  - 3.1.2 Detector energy resolution 25
  - 3.1.3 Contrast-enhanced spectral imaging 26
  - 3.1.4 * Unenhanced spectral imaging 28
- 3.2 Results and Discussion 30
  - 3.2.1 Detector energy resolution 30

3.2.2 Contrast-enhanced spectral imaging 31
3.2.3 * Unenhanced spectral imaging 35

4 Conclusions and Outlook 41
4.1 X-Ray Optics in Mammography 41
4.2 Spectral Imaging 42

Acknowledgements 45

Bibliography 47

Chapter 1

Introduction

1.1 Breast Cancer and Mammography Screening

Breast cancer is by far the most common form of cancer among women, and the second most common cause of cancer death in Sweden, the European Union, and the United States [1–3]. The lifetime risk of being diagnosed with breast cancer is approximately 10%, and 3% of all women die from the disease.

Preventing breast cancer is difficult because the causes of the disease are largely unknown. Detecting the cancer early, while it is still local and has not metastasized is essential for successful treatment [4]. The only way to achieve early detection in a large population today is with screening mammography. Survival rates among breast cancer patients in western Europe, Australia, and the Americas have been increasing since the beginning of the 1990s, at least in part as the result of widespread screening programs. Positive effects of breast cancer screening were reported already in the early 1970s [5], and have been reaffirmed by several studies since. For instance, a randomized controlled trial measured a 50% reduction in mortality among women participating in a Swedish mammography program [6].

Several difficulties are associated with imaging the breast, making mammography one of the most technically demanding radiographic techniques [7]. Imaging of relatively large, low-contrast tumors requires a high contrast-to-noise ratio, which translates into a need for efficient scatter rejection, and low-noise image receptors. Further, the variability of the anatomical background acts as nearly random noise, which reduces detectability [8, 9]. On the other extreme is imaging small high-contrast microcalcifications, one of the early signs of breast cancer, which puts high demands on spatial resolution.

In addition, the radiation dose used in screening mammography must be tightly constrained because of the large number of women exposed. No direct evidence has established the oncogenicity of low-level ionizing radiation from medical x-ray imaging, but a linear, non-threshold extrapolation from higher doses is widely accepted [10, 11], *i.e.* cancer risk is proportional to radiation dose. For example, it has been estimated for the UK breast screening program that 1 case of breast cancer is inducted for each 24 to 27 cases detected among women aged 44 to 49 years [12]. The ratio increases with age, and the benefit of mammography, at least for older women, is unquestionable. Nevertheless, minimizing the dose is still essential.

Ultrasonography and magnetic resonance imaging (MRI) are superior to x-ray mammography in some cases, *e.g.* to detect certain lobular invasive carcinomas and to distinguish between solid and cystic lesions [4]. Ultrasonography is, however, time-consuming and highly operator-dependent, whereas MRI is costly and usually requires contrast-enhancement. Therefore, these techniques may be used mainly for diagnostic mammography and as an adjunct to x-ray imaging for young women at high risk of hereditary breast cancer and for women with dense breast tissue. X-ray mammography is expected to continue to be the dominating screening modality because of its relatively low complexity and high spatial resolution [13].

1.2 Digital Mammography

1.2.1 From film, over energy integration, to photon counting

Traditional screen-film mammography has superior spatial resolution, and, although digital technology potentially performs better in terms of dose, contrast resolution, and dynamic range, it was not until a large trial in 2005 had shown equal or better clinical performance that digital mammography became widely accepted [14]. The proportion of digital mammography units has since increased, and at the time of this writing was 58% in the United States [15] and almost 90% in Scandinavia.

Digital radiography was initiated with computed radiography systems [7, 13, 16]. These systems are based on a cassette of storage phosphor instead of film, and the recorded x-rays are readout post-exposure by a laser. Computed radiography systems were investigated in the 1980s for mammography, but the spatial resolution was not sufficient for routine clinical use, and not until flat-panel detectors were introduced did digital mammography become feasible. Indirect flat panels have an array of photodiodes that record the light from a cesium-iodide scintillator. Although cesium iodide can be manufactured with a columnar structure to guide the light, some spreading still remains and degrades resolution. Instead, direct flat panel detectors have a photoconductor of amorphous selenium deposited on top of an array of thin-film transistors, which record the charge that is released in the selenium layer upon photon interaction. The diffusion of charge is less than the spreading of light, so direct detectors provide higher resolution.

In the technologies mentioned above, the charge released at each photon conversion is summed over the exposure time. Flat-panel detectors, for instance, have storage capacitors at each pixel that accumulate the charge. Because the released charge at photo absorption is proportional to photon energy, these detectors are referred to as "energy integrating." Obviously, high-energy photons are assigned a higher weight, which is arbitrary, and any electronic noise present in the pixels is integrated with the signal, which adds uncertainty. Photon-counting detectors, on the other hand, have electronics that are fast enough to count individual photons as they are converted in the detector material. All photons are hence assigned the same weight, and electronic noise can be eliminated by setting a threshold. Moreover, by implementing several thresholds, the detectors can be made energy sensitive.

Photon-counting detectors have been employed in nuclear medicine for decades, but their introduction in x-ray imaging was delayed, mainly as a result of the higher flux encountered. In fact, because of the relatively low count rates per pixel, the first commercial photon-counting application was a mammography system, which was introduced by Sectra Mamea AB in 2003. This system is based on silicon strip detectors that are similar to those used for high-energy physics experiments [17–20] and is described in some detail in the next section. Other photon-counting mammography detectors with linear or area configurations and based on gas, silicon, cadmium-zinc telluride (CZT), or gallium arsenide are being developed or investigated by commercial companies and research groups [21–27]. The advantages of silicon include a high charge-collection efficiency and virtually no fluorescence compared to high-Z solid-state detectors, as well as a high efficiency relative to gas detectors. In addition, the ready availability of high-quality silicon crystals, and the established methods for test and assembly should not be underestimated. The low absorption efficiency of silicon is usually compensated for by arranging the silicon wafers edge on [17, 22].

1.2.2 Photon-counting detectors in a multi-slit geometry

Much of the work in this thesis is based on the Sectra MicroDose Mammography system. Briefly, the system consists of a tungsten-target x-ray tube with aluminum filtration, a pre-collimator, and an image receptor, all mounted on a common arm (Fig. 1.1, Left). The image receptor consists of several modules of silicon strip detectors with corresponding slits in the pre-collimator (Fig. 1.1, Right), and the Sectra system will henceforth be referred to as a multi-slit system. To acquire an image, the arm is rotated around the center of the source so that the detector modules and pre-collimator are scanned across the object. A detailed description of the detector and readout electronics is found in Chapter 3.

1.2.3 Beam focusing with x-ray optics

Multi-slit systems have the advantage of efficient intrinsic scatter rejection [19, 28], but a relatively large amount of radiation is blocked before the object by the pre-collimator. High tube loadings or longer acquisition times might follow, and the available photons need to be used more efficiently. X-ray optics have been suggested as one option to improve photon economy. As an alternative to conventional grids or air gaps, capillary optics can be placed in bundles after the object to reduce scattered radiation and to improve resolution [29]. The size of the field is, however, limited by manufacturing constraints, and primary quanta are still

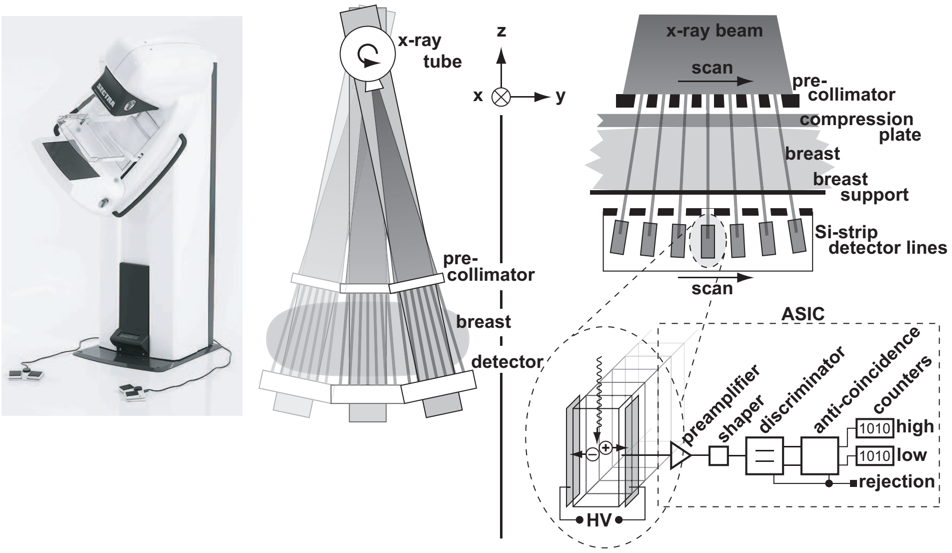
x-ray
tube
z
x
y
pre-
collimator
breast
detector
x-ray beam
scan
pre-
collimator
compression
plate
breast
breast
support
Si-strip
detector lines
scan
ASIC
preamplifier
shaper
discriminator
anti-coincidence
counters
1010 high
1010 low
rejection
HV

Figure 1.1: **Left:** Photograph and schematic of the Sectra MicroDose Mammography system [image courtesy Sectra Mamea AB]. **Right:** The image receptor and electronics.

absorbed. Capillaries can also be used to gather radiation before the object [30], but divergence of the radiation at the exit side distorts the resolution so that the capillaries need to be combined with a diffracting crystal; the capillaries increase the flux to the crystal and the limited acceptance angle of the crystal reduces the divergence of the beam.

Another approach is to use an array of refractive x-ray lenses as a focusing pre-object collimator that reduces the divergence of the beam [Paper II]. This technique is referred to as *beam focusing*, and it is investigated in some detail in Chapter 2. Refractive lenses can be expected to have a less-negative effect on the resolution than capillary optics, and are convenient from a manufacturing point of view.

1.3 The X-Ray Energy Spectrum

Mammography generally refers to imaging in the lower part of the hard x-ray region. Figure 1.2 (Left) shows a typical incident spectrum (30 kVp tungsten anode and 0.5 mm aluminum filtration [31, 32]). Here, x-ray interaction with matter is dominated by the photoelectric effect and Compton scattering, as is illustrated in Fig. 1.2 (Right) for adipose and glandular tissue [32, 33]. Absorption increases rapidly at lower energies because of the photoelectric effect, which results in a higher radiation dose to the patient and fewer photons that reach the detector.

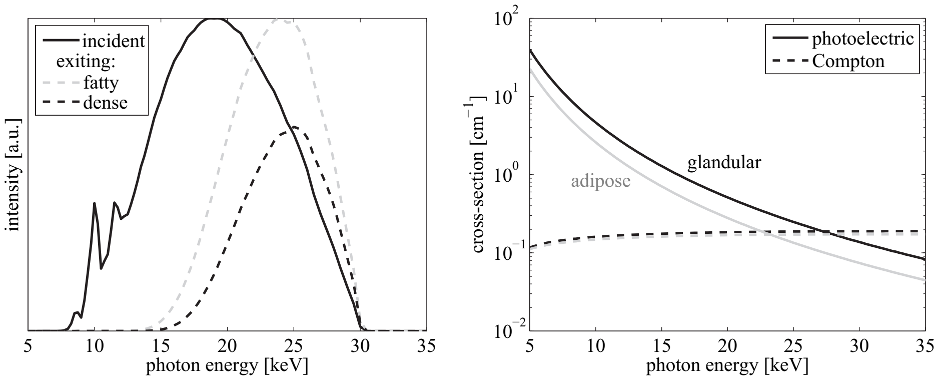

Figure 1.2: **Left:** Typical mammography spectra that are incident on, or have passed (exiting) averaged-sized breasts of two different compositions. The exiting spectra are normalized and do not show the attenuation relative the incident spectrum. **Right:** The photoelectric and Compton cross-sections for adipose (gray) and glandular (black) tissue. The Compton cross-sections almost coincide.

Nevertheless, the photons that actually do get through the object have more contrast information as a result of larger attenuation differences and a relatively small scattering component. Accordingly, for a certain object, there is an optimum in incident photon energy to maximize contrast and to minimize quantum noise and dose [34].

For a given incident x-ray spectrum, however, photons that hit the detector can be wisely used by assigning a greater weight to the information-dense, low-energy photons [35, 36]. Moreover, the two tissue types in Fig. 1.2 (Right) have different proportions of photoelectric and Compton components (the photo-electric cross-sections differ while the Compton cross-sections almost coincide), and it is evident that the energy dependence of x-ray attenuation is material-specific [37, 38]. This fact is also illustrated in Fig. 1.2 (Left) where the spectra through different breast compositions differ, not only in intensity, but also in shape. Hence, the detected energy spectrum can be used to extract information about the object composition.

We conclude that there are two components of spectral mammography as defined here; (1) optimizing the incident energy spectrum, which is referred to as *spectral shaping*, and (2) utilizing the information in photons that have already passed through the object by energy-resolved detection, which is referred to as *spectral imaging*.

1.3.1 Spectral shaping with x-ray optics

Spectral shaping is also known as energy filtering, and its positive effects were observed already at the advent of medical x-ray imaging. It was noted that putting a thin material, such as a piece of leather, between the patient and the x-ray tube reduced irritation of the patient's skin [39]. Energy filtering has subsequently been refined for mammography [40–42], but the technology has not changed greatly over the years; absorption filtering is still the dominant method to filter out low-energy photons, often in combination with a limited x-ray tube acceleration voltage to cut off higher-energy photons. In some cases the material of the absorption filter is chosen so as to have an absorption edge above the optimal energy to further reduce the high-energy part of the spectrum. In principle, the spectrum can be made arbitrarily narrow by heavy filtration, but only at the cost of a severe reduction in flux.

To optimize the spectrum beyond the practical limit of absorption filtering, several options have been proposed. Synchrotrons [43–45], and some other exotic x-ray sources [46–49] are capable of producing nearly monochromatic beams. Authors have reported promising results on dose efficiency, but the high complexity and cost of such sources limit the feasibility for routine clinical x-ray imaging.

Instead, filtering applied to conventional x-ray tubes is desirable, but the relatively low photon yield becomes a problem if a large part of the spectrum is removed. Mosaic crystals with small imperfections in the structure have a higher reflectivity than perfect crystals and yield a narrower spectrum than absorption filters, which may be a suitable compromise for mammography [50, 51]. Spatial resolution in the plane of diffraction is decreased, however, and the available flux is still lower than it is in conventional mammography. The lower flux can be mitigated to some extent by using polycapillary optics to gather the radiation into a quasi-parallel beam [30]. A second option along the same avenue is to use curved crystals, which are claimed to have a larger acceptance angle, better energy resolution, and less effect on the spatial resolution than mosaic crystals [52].

A different approach is to use refractive, chromatic x-ray lenses [53, Papers I, III, IV]. These lenses are inserted inline and therefore do not change the imaging geometry to the same extent as crystals do, and the line foci of the lenses are ideal for coupling to the strip detectors of the multi-slit system. Results for spectral shaping with x-ray lenses are summarized in Chapter 2.

1.3.2 Spectral imaging with a photon-counting detector

Spectral imaging in mammography has at least three potential benefits:

1. Energy weighting refers to optimizing the signal-to-quantum-noise ratio with respect to its energy dependence; photons at energies with larger agent-to-background contrast can be assigned a greater weight [35, 36].

2. Dual-energy subtraction refers to optimizing the signal-to-anatomical-noise ratio by minimizing the background clutter contrast. The contrast between any two materials (adipose and glandular tissue) can be eliminated in a weighted subtraction of different-energy acquisitions, whereas all other materials (lesions) to some degree remain visible as a result of the different energy

dependencies of the attenuation. This technique has been investigated for imaging tumors [54–56] and microcalcifications [57–64]. In the case of tumors, contrast agents can be used for enhancement because angiogenesis leads to increased permeability [65]. If the agent material has an absorption edge in the energy interval, the contrast in a subtracted image can be greatly improved by the steep energy dependence of the attenuation [24, 66–69]. Compared to temporal subtraction [67, 70, 71], dual-energy subtraction may yield lower contrast and less-efficient background subtraction, but it is not as prone to motion artifacts.

3. Energy weighting and dual-energy subtraction both aim to increase the ability to detect lesions. A third possible benefit of spectral imaging, which is the focus of much investigation in energy-resolved CT, is the ability to extract information about the target material, *e.g.* differentiation or quantification [37, 72, 73]. An example in mammography is to evaluate microcalcification thickness [63].

One way of obtaining spectral information about the object is to use two or more input spectra. For imaging with clinical x-ray sources, this approach often translates into several exposures with different beam qualities (different acceleration voltages, filtering, and anode materials) [58, 66, 67]. Results of the dual-spectra approach are promising, but the examination may be lengthy, which leads to an increased risk of motion blur and discomfort for the patient. This problem can be solved by a simultaneous exposure with different beam qualities [69], or by using an energy-sensitive sandwich detector [60, 61]. For all of the above approaches, however, the effectiveness may be impaired by overlap in the spectra and by a limited flexibility in choice of spectra and energy levels.

In recent years, photon-counting silicon detectors with high intrinsic energy resolution, and, in principle, an unlimited number of energy levels (electronic spectrum-splitting) have been introduced as another option [24, 68, Papers V, VI]. This approach is discussed further in Chapter 3.

1.4 Outline of the Thesis and Connection to Previous Work

The original purpose of this thesis was to study spectral shaping in mammography with two types of refractive x-ray lenses that were originally developed by Björn Cederström [74]. Results from simulations of the lenses, and measurements with x-ray tubes and synchrotron radiation are presented in Papers I and III and are summarized in Chapter 2. Paper IV ties these two studies together with an investigation of the potential dose-reduction for spectral shaping.

The idea was to couple the line foci of the one-dimensional x-ray lenses to line-shaped silicon strip detectors, and, subsequently, the scope of the thesis was extended to incorporate more of the detector part in the analysis. Much of the work in this latter part of the thesis was done in collaboration with Sectra Mamea AB and the HighReX EU-project [75]. The photon-counting detectors were originally developed by Mats Lundqvist [76], and were characterized in terms of implementation in a multi-slit geometry for full-field digital mammography by Magnus Åslund [77].

A study of using x-ray lenses to improve photon economy in the multi-slit geometry (beam focusing) is presented in Paper II and summarized in Chapter 2. Lens simulations are compared to measurements. The last part of the thesis, Chapter 3, presents a study of the photon-counting detectors for spectral imaging, which builds on earlier work by Hans Bornefalk [78]. In Paper V, a detector model is developed and benchmarked to measurements. Paper VI employs the model to investigate the feasibility of contrast-enhanced spectral imaging with the system. Chapter 3 additionally presents a study on spectral imaging without contrast agent. These results have not yet been published, and are indicated by an asterisk in the section titles. A few smaller complements to the results in the papers have been added throughout the thesis and are not indicated.

1.5 Author's Contribution

The author is the primary and most often the sole contributor to the research results presented in this thesis. It should, however, be recognized that the measurements and simulations at several instances have depended on specific contributions by others. The lenses used in Paper I were supplied by Carolina Ribbing and Björn Cederström. In Paper II, Staffan Karlsson coordinated lens fabrication, and Peter Nillius developed some of the ray-tracing algorithms. The synchrotron measurements in Paper III were carried out by Björn Cederström, Peter Nillius, Staffan Karlsson, and the Author. Mats Lundqvist contributed the simulated data for charge sharing in Paper V. The silicon strip detector unit that was used in Paper II, and for some of the measurements in Paper V was set up by Alexander Chuntonov. Magnus Hemmendorff assisted with data readout from the detector array in Papers V and VI. General contributions by several other people are listed in the Acknowledgements.

Chapter 2

X-Ray Optics

2.1 Materials and Methods

2.1.1 Background

Refractive focusing of x rays is difficult because the refractive index is very close to unity; a lens would need a cumbrously small radius of curvature, and diffractive and grazing incidence optics were for long the sole alternatives [79, 80]. If the weak refractive effect is divided over a large number of surfaces, however, refractive lenses can be manufactured with reasonable curvatures even for hard x-rays. This was first realized with the compound refractive lens (CRL), where the series of surfaces ideally are parabolic [81, 82].

A modification of the CRL is the multi-prism lens (MPL), which consists of two rows of prisms put on an angle in relation to the optical axis [74, 83, 84]. Hence, the MPL is built up of only flat surfaces, which simplifies manufacturing, and in addition, the focal length is tunable by changing the angle between the lens halves. Figure 2.1 illustrates that the projection of the two prism rows of the MPL approximates a parabola with straight line segments. It is a planar lens and therefore focuses radiation into a line focus.

The parabolic profiles of CRLs and MPLs lead to rapidly increasing absorption towards the periphery of the lens, which limits the usable aperture, and hence the efficiency. One way to increase lens transmission is to use Fresnel representations with lens material corresponding to a phase shift of integer steps of 2π removed. This strategy was first proposed and realized for parabolic lenses and CRLs [85–87]. These lenses do, however, suffer from a rapid decrease in feature size towards the periphery, which sets a practical limit for the aperture, similar as for zone plates at hard x-ray energies

A Fresnel version of the MPL avoids high aspect ratios and provides uniform features throughout the lens, which simplifies manufacturing [88, 89]. In the prism-array lens (PAL), each prism in the MPL is exchanged for a column of smaller prisms as is illustrated in Fig. 2.1. The focal lengths are the same if the prism angle (θ) and

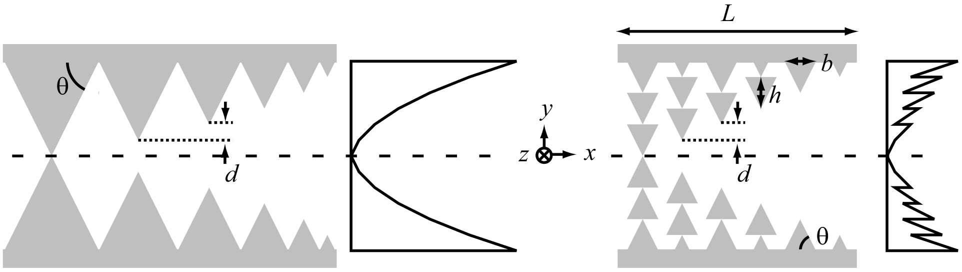

Figure 2.1: The transition from MPL to PAL. **Left:** The MPL approximates a parabolic profile by straight line segments. **Right:** In a PAL, each prism in the MPL is exchanged for a column of smaller prisms, resulting in a shorter lens with lower absorption.

the columnar displacement (d) of the two lenses are equal, and the base (b) of each small prism corresponds to an integer number of 2π phase shifts. The projection of the PAL approximates a Fresnel lens, superimposed on a linear profile, where the latter constitutes a cost in absorption compared to an ideal Fresnel lens.

Considerations in choice of lens material are similar for MPLs and PALs. Somewhat simplified, low-Z materials, such as beryllium and lithium, are advantageous from an absorption point of view [90, 91], silicon provides manufacturing convenience [92, 93], and diamond is ideal for high-brilliance synchrotron applications [92, 94]. For small-scale applications, which are considered in this work, polymers constitute a suitable compromise between atomic number ($Z \approx 6$), and availability and handling convenience. Epoxy MPLs can be manufactured by molding or UV embossing on silicon masters, which are in turn produced by anisotropic etching so that the $< 111 >$ lattice planes define the prism sides [90, 92, Paper II]. Fine machining of PMMA and vinyl has also been pursued, but with a slightly poorer result [53, 83].

The type of PAL considered in this thesis has only been manufactured by etching in silicon [88, Paper III]. Similar lenses have, however, been fabricated with encouraging results in PMMA and SU-8 using deep x-ray lithography according to the LIGA process (Lithographie, Galvanoformung, Abformtechnik) [95, 96]. In summary, an intermediate mask is created by UV photolithography and electroplated with a metal. The intermediate mask is then, in a similar manner, used to create a thicker working mask with soft x-ray lithography. The working mask is finally employed for lithography in relatively thick substrates of PMMA or SU-8. Aspect ratios in the order of 1:25 – 1:50 have been obtained with depths of several hundreds of micrometers and surface roughness less than 50 nm in both materials. SU-8, however, exhibits slightly better fabrication results and radiation resistance, and is likely the preferable candidate for x-ray lenses.

There are at least two different ways that an MPL or PAL can be employed in the multi-slit geometry: (1) as an energy filter to optimize the x-ray spectrum, and (2) as a focusing pre-object collimator that reduces the divergence of the beam and increases utilization of the available x-rays compared to a slit collimator. A decisive advantage of using planar refractive lenses in the multi-slit geometry is that the one-dimensional focus matches the shape of the silicon strip detectors in the multi-slit geometry.

2.1.2 Spectral shaping

MPL versus PAL

Lens properties with respect to spectral shaping with MPLs and PALs are discussed in Papers I and III, respectively. The focal lengths of the lenses are

$$F_{\mathrm{MPL}} = \frac{d_{\mathrm{g}} d_{\mathrm{t}}}{\delta L} = \frac{d \tan\theta}{2\delta}, \tag{2.1}$$

$$F_{\mathrm{PAL}}^{\mathrm{ref}} = \frac{dh}{\delta b} = \frac{d \tan\theta}{2\delta}, \quad \text{and} \quad F_{\mathrm{PAL}}^{\mathrm{diff}} = \frac{dh}{\lambda}, \tag{2.2}$$

where d_{t}, d_{g}, and L are the tooth height, gap at the rear end, and length of the MPL; h and b are the prism height and base of the PAL; d and θ are the successive columnar displacement and prism angle for each lens; δ is the deviation of the refractive index from unity and λ is the x-ray wave length. F_{MPL} and $F_{\mathrm{PAL}}^{\mathrm{ref}}$ were found by assuming parabolic projections of lens material [84, 88], and written this way we see that they are equal if the two lenses have the same prism angles and successive displacements. $F_{\mathrm{PAL}}^{\mathrm{ref}}$ has restricted validity, however, as diffractive effects are not considered, and $F_{\mathrm{PAL}}^{\mathrm{diff}}$ was derived by assuming a series of blazed phase gratings [Paper III]. At the design energy of the PAL, b corresponds to an integer phase shift of 2π, and $F^{\mathrm{diff}} = F^{\mathrm{ref}}$, *i.e.* the blazing condition is fulfilled. Away from the design energy, however, it is shown in Paper III that F^{diff} dominates. Because $\delta \propto E^{-2}$ in the hard x-ray region, and $\lambda \propto E^{-1}$, both lenses are chromatic with approximate focal lengths

$$F_{\mathrm{MPL}} \propto E^2 \quad \text{and} \quad F_{\mathrm{PAL}} \propto E, \tag{2.3}$$

where E is the photon energy. Hence, a slit placed in the image plane of a particular x-ray energy will transmit radiation of that energy, whereas other parts of a polychromatic incident beam are out of focus and preferentially blocked. This setup is outlined in Fig. 2.2 (Center), and we refer to it as a filter. Similar filters have been investigated in the soft x-ray region with Fresnel zone plates [97, 98], and in the hard x-ray region with MPLs [53].

Efficiency, and resolution properties of the filter depend on the transmission and aperture of the lens. The transmission function (η) is a Gaussian for an MPL [84], and exponentially decreasing towards the periphery for a PAL [88]. If rewritten

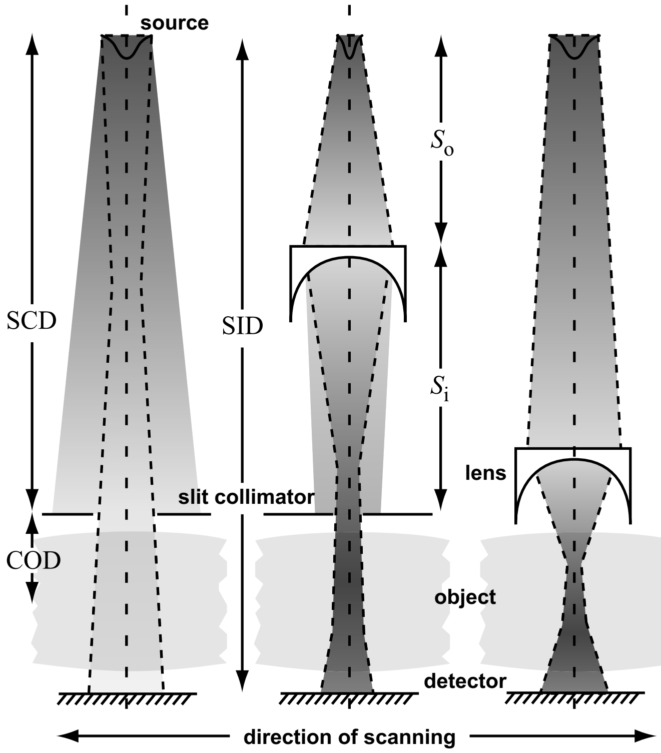

Figure 2.2: Schematics of the filtering (Center) and the collimator (Right) geometries for x-ray lenses. To the left is the standard slit geometry that is similar to the one in Fig. 1.1. Note that none of the distances are to scale.

from the previous reports to facilitate comparison,

$$\eta_{\mathrm{MPL}}(y) = \exp\left(-y^2 \frac{\mu}{2\delta F}\right) \quad \text{and} \quad \eta_{\mathrm{PAL}}(y) = \exp\left(-|y| \frac{h}{4} \frac{\mu}{2\delta F}\right), \tag{2.4}$$

where μ is the linear attenuation coefficient of the lens material. We see that $\eta_{\mathrm{PAL}} > \eta_{\mathrm{MPL}}$ for $|y| > h/4$, which is always the case in practice. In fact, for $|y| < h$, $\eta_{\mathrm{PAL}} = \eta_{\mathrm{MPL}}$, which is not seen in Eq. (2.4) because of the approximations involved. The effective aperture (D_{e}) is the transmission function integrated over the physical aperture, and can be interpreted as the width of a slit with the same transmission as the lens. Hence, for infinitely large lenses, which is often a good approximation,

$$[D_{\mathrm{e}}]_{\mathrm{MPL}} = \sqrt{\pi \frac{2\delta F}{\mu}} \quad \text{and} \quad [D_{\mathrm{e}}]_{\mathrm{PAL}} = \frac{4}{h} \frac{2\delta F}{\mu}. \tag{2.5}$$

The transmission of lens is $t = D_\mathrm{e}/D_\mathrm{p}$. Together with the image distance, the effective aperture determines the numerical aperture, which in turn determines the wave-length-dependent diffraction-limited resolution of the lens. For all cases in this thesis, however, we are source limited rather than diffraction limited, and this issue is not considered further.

Assuming a Gaussian source, an infinitely large lens, and a slit width equal to the image size, the gain as a function of energy for the MPL [84] and PAL [Paper III] are

$$\begin{aligned} G_\mathrm{MPL} &= \frac{D_\mathrm{e}}{F}\frac{s_\mathrm{o}}{d_\mathrm{o}} = 2.5 \times \frac{s_\mathrm{o}}{d_\mathrm{o}}\sqrt{\frac{1}{F}\frac{\delta}{\mu}} \quad \text{and} \\ G_\mathrm{PAL} &= \frac{D_\mathrm{e}}{F}\frac{s_\mathrm{o}}{d_\mathrm{o}} \times 0.76 = 3.0 \times \frac{s_\mathrm{o}}{d_\mathrm{o}}\frac{1}{h}\frac{\delta}{\mu}, \end{aligned} \tag{2.6}$$

where s_o is the source-to-lens distance and d_o is the source size. Hence,

$$\frac{G_\mathrm{PAL}}{G_\mathrm{MPL}} = 0.86 \times \sqrt{\frac{\delta}{\mu}\frac{1}{\lambda}\frac{1}{\gamma}} = 1.7 \times \sqrt{\frac{\delta^3}{\mu}\frac{1}{\lambda^2}\frac{F}{\tan^2\theta}}, \tag{2.7}$$

where $\gamma = h/d \geq 1$. Since θ is likely limited by physical constraints, the most realistic approach to optimize lens performance is to keep F and θ fixed, which corresponds to the second expression in Eq. (2.7) and implies that d varies. We recall that $\delta \propto E^{-2}\rho$ away from any absorption edges, $\mu \propto E^{-3}Z^{3.2}\rho$ at low energies and negligible Compton scattering, and $\mu \propto \rho$ at high energies and negligible photo absorption [84]. Hence, $G_\mathrm{PAL}/G_\mathrm{MPL} \propto E^{-0.5}Z^{-1.6}\rho$ at low energies, and $G_\mathrm{PAL}/G_\mathrm{MPL} \propto E^{-2}\rho$ at high energies. The benefit of the PAL decreases monotonically with energy. At low energies, the benefit is largest for light materials, but at higher energies, the PAL is more advantageous for dense lens materials because of the higher refractive index. These observations are confirmed by Fig. 2.3, which plots $G_\mathrm{PAL}/G_\mathrm{MPL}$ for some potential lens materials at mammography energies. In this case, $F = 200$ and $\tan\theta = 0.1$, and the data range is for $\gamma \geq 1$. For plastics, using a PAL is clearly worthwhile at mammography energies, whereas for lighter and heavier materials, the extra effort compared to the MPL may be questioned. Material and energy dependence of the gain (Eq. (2.6)) has been investigated previously for MPLs [84] and PALs [88]. In general, it was found that low-Z materials are more beneficial at low energies, in particular for the PAL. At higher energies the material dependence vanishes for the MPL, and is reversed for the PAL. Also note that other lens and material properties may need to be considered in an optimization, for example, the lens length is minimized for dense materials, light materials may be difficult to machine and handle, and radiation hardness is material dependent.

Under the same assumptions as the gain in Eq. (2.6), the energy resolution was derived for the PAL filter in Paper III, and, with slight modifications, for the MPL filter in a previous study [74];

$$\left[\frac{\Delta E}{E}\right]_\mathrm{MPL} = \frac{1.7}{G_\mathrm{MPL}}, \quad \left[\frac{\Delta E}{E}\right]_\mathrm{PAL} = \frac{2.6}{G_\mathrm{PAL}} \quad \Rightarrow \quad \frac{\Delta E_\mathrm{MPL}}{\Delta E_\mathrm{PAL}} = 0.65 \times \frac{G_\mathrm{PAL}}{G_\mathrm{MPL}}, \tag{2.8}$$

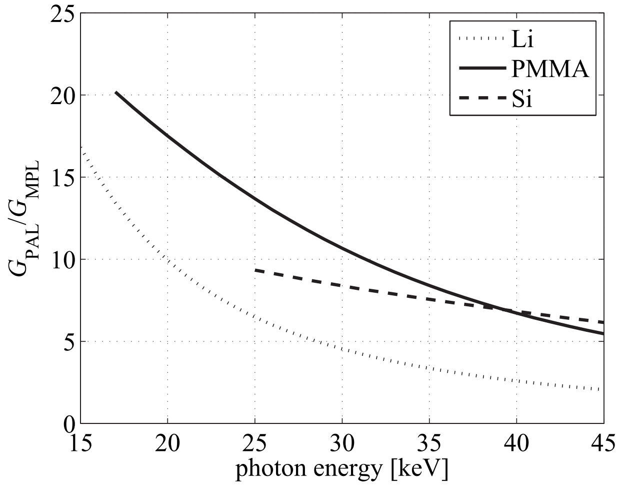

Figure 2.3: The benefit of the PAL in terms of gain for lithium, PMMA, and silicon lenses in the mammography energy range for a fixed focal length and prism angle (θ), which implies that the columnar displacement (d) varies.

where ΔE is the FWHM of the gain peak. Hence, we see that the MPL filter can be expected to be superior to the PAL filter in terms of energy resolution at equal gain because of the higher energy dependence of the focal length, but, again, the asset of the PAL filter is the potentially higher gain according to Eq. (2.7) and Fig. 2.3.

It should also be noted that the transmitted energy of the MPL filter is tunable by changing the angle between the lens halves. This flexibility is sacrificed in the PAL filter, which is designed for a particular x-ray energy. On the other hand, the PAL is shorter, which may be advantageous in small-scale applications because of the shorter setups involved. The length of the MPL can be reduced somewhat by a successively decreasing prism height instead of tilted lens-halves [Paper II], which is illustrated in Fig. 2.1. This modified lens is referred to as a compact MPL (C-MPL), and is only slightly tunable. The lengths of the MPL, C-MPL, PAL, and for comparison a parabolic lens, are

$$L_{\mathrm{MPL}} = \frac{D_{\mathrm{p}}^2}{F\delta}, \quad L_{\mathrm{C\text{-}MPL}} \approx \frac{D_{\mathrm{p}}^2}{2F\delta}, \quad L_{\mathrm{PAL}} = \frac{D_{\mathrm{p}}h}{F\delta}, \quad \text{and} \quad L_{\mathrm{para}} = \frac{D_{\mathrm{p}}^2}{2F\delta}, \tag{2.9}$$

where D_{p} is the physical aperture. We note that the length of the MPL is twice that of the C-MPL and the parabolic lens, and that the PAL is shorter than any of the other lenses for all practical apertures.

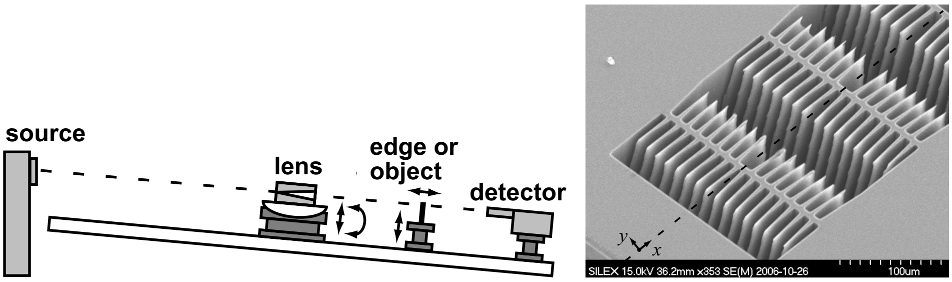

Figure 2.4: **Left:** The experimental setup that was used for lens measurements. The lens is either an MPL or a PAL, and the detector is a 128-channel silicon strip detector or a CZT spectrometer. The source size could be tuned with the angle of the setup. **Right:** SEM image of the experimental PAL.

Focusing and filtering

A test bench for lenses according to Fig. 2.4 (Left) was assembled and used for some of the measurements. The source was a tungsten-target x-ray tube with 10 – 60 kV acceleration voltage. A large range of horizontal source sizes were available, and the size could be additionally tuned with the angle of the setup. The detector was either a 128-channel silicon strip detector, which is described in some detail in Chapter 3, or a CZT compound solid-state detector connected to a multi-channel analyzer.

Paper I describes a geometrical model under the thin-lens approximation, and a ray-tracing framework for the MPL. Further, an epoxy lens-half with an aperture of 100 μm [92] was evaluated experimentally on the test bench with a 24 μm source. Energy-resolved beam profiles were recorded with a scanned edge device and the CZT detector. More details on the lens and setup are given in Table 2.1.

A preliminary study suggested that ray-tracing of a PAL filter differs substantially from measurements and physical-optics calculations [99], and it seemed that geometrical optics cannot be directly applied to find the energy resolution because the focal length is not predicted correctly. Nevertheless, a geometrical model based on the approximate expression for the focal length in Eq. (2.3) was developed in Paper III and compared to a thorough field-propagation model. In addition, a 200-μm-aperture silicon PAL with a design energy of 23 keV was manufactured and evaluated experimentally on the test bench with a similar procedure as for the MPL. An image of the experimental PAL is shown in Fig. 2.4 (Right).

The PAL was manufactured with relatively steep prism angles, and the gain may be reduced by phase errors caused by roughness on the large number of traversed surfaces. Surface roughness has not yet been implemented in the field-propagation model, but assuming uncorrelated Gaussian phase errors, an approximate expression for the reduction in peak intensity for the PAL can be derived in accordance with previous studies [100];

$$\eta_{\mathrm{r}}(y) = \exp\left[-\left(2\pi\frac{\delta}{\lambda}\right)^2 \sum \sigma_x^2\Big|_y\right], \quad \text{where} \quad \sum \sigma_x^2\Big|_y = \frac{\sigma_{\mathrm{t}}^2}{d}\left(\frac{y}{\tan^2\theta} + D_{\mathrm{p}}\right). \tag{2.10}$$

σ_x and σ_{t} are the roughness standard deviations of the individual surfaces in the directions of the wave and tangential to the surface, respectively, and D_{p} is included because it determines the number of support structures.

Implementation in a clinical setup

Paper I presents a model to compare an MPL-filtered system with an absorption filtered reference system in terms of dose and signal-to-noise ratio, and with spatial resolution, exposure time, and imaging geometry as constraints. In Paper IV, the model is substantially improved, and extended to include also the PAL filter.

The geometries for comparison of lens- and absorption-filtering are outlined in Fig. 2.2, and are referred to as the lens and reference geometries. A full system consists of an array of either of these in a multi-slit assembly. Equal dimensions were chosen for the two setups with a source-to-image distance (SID) of 750 mm. A mammographic tungsten spectrum was assumed, and the reference system was filtered with 0.5 mm aluminum. Transmitted spectra of epoxy MPL and PAL filters were calculated using the geometrical models in Papers I and III. The prism angles were kept fixed and equal to the experimental lenses in order to ensure manufacturing feasibility. A maximum lens length of 40 mm constrained the aperture for a certain focal length.

A 50% glandularity breast with an embedded 300 μm calcification was assumed. The optimal spectrum is fairly independent of lesion type, and the results should be similar for masses [76, 101]. The spectral quantum efficiency (SQE) was used as a figure of merit for the benefit of energy filtering [42];

$$\mathrm{SQE} = \frac{\mathrm{SDNR}^2}{\mathrm{AGD}} \cdot \frac{\mathrm{AGD}_{\mathrm{mono}}}{\mathrm{SDNR}^2_{\mathrm{mono}}}, \tag{2.11}$$

where SDNR is the signal-difference-to-noise ratio, AGD is the average glandular dose, and subscript *mono* indicates the ideal monochromatic case.

The resolution in the detector-strip direction is unaffected by the lens. In the scan direction, however, the lens-filtered system has a modulation transfer function (MTF) that is given by

$$T = T_{\mathrm{aperture}} \times T_{\mathrm{image}} \times T_{\mathrm{scan}} \times T_{\mathrm{add}}. \tag{2.12}$$

In this cascade, T_{aperture} is the contribution by the lens aperture, which is the Fourier transform of the lens transmission function, scaled by a factor $\mathrm{COD}/s_{\mathrm{i}}$, where COD is the collimator-to-object distance, and s_{i} is the lens-to-collimator distance. T_{image} is the MTF contribution from the image of the source, which is a sinc function if we assume a rectangular source, scaled by a factor $s_\mathrm{i}/s_\mathrm{o} \times (\mathrm{COD} + s_\mathrm{i})/s_\mathrm{i}$, where s_o is the source-to-lens distance. T_scan and T_add are the contributions from the scan step, and from misaligned detector units, which are both sinc functions, scaled by a factor $(\mathrm{SCD} + \mathrm{COD})/\mathrm{SID}$ to compensate for the fact that the detector is rotating around the source and not linearly scanned. The resolution of the reference system is determined correspondingly by the source, the slit, the scan step, and misaligned detector units [76].

2.1.3 Beam focusing

The second perceivable lens geometry is to replace the pre-object multi-slit collimator with an array of lenses that reduces the divergence of the beam and hence increases utilization of the available x-rays (Fig. 2.2). Beam focusing was evaluated in Paper II with an epoxy C-MPL, consisting of two lens halves glued together for a 140 μm aperture with optical fibers as spacers. 606 prisms with $\theta = 54.7°$ yielded $F = 180$ mm at 18 keV. The test bench with a source size of 425 μm and the silicon strip detector was used for experimental evaluation, and comparison to a slit geometry with equal beam quality. Source-to-lens and source-to-image distances were 507 and 640 mm, which is feasible for a clinical setup. Ray-tracing simulations were compared to measurements and used to predict performance.

Flux and spatial resolution are coupled in a collimator geometry, and both these parameters were measured in the comparison between lens and slit systems. In addition, phantom images were acquired with the setup.

2.2 Results and Discussion

2.2.1 Spectral shaping

Focusing and filtering

Figure 2.5 (Left) shows the MPL-filtered spectrum at a peak energy of 20 keV along with the unfiltered tungsten spectrum. These curves yield the intensity gain by division, with the result shown in Fig. 2.5 (Right) together with model predictions. Tunability was verified by altering the angle between the lens-halves to achieve peak energies of 17, 20, and 23 keV. The measured gain over a 10 μm slit of 5.9 – 6.6 was in good agreement with the ray-tracing and geometrical models. Table 2.1 summarizes some of the parameters from the measurements and simulations for the 23 keV peak. The transmission of the lens was more than 50%, but the aperture was fairly small, and the transmission would decrease for a larger-aperture lens. The measured energy resolution was found to be approximately constant for the three peaks.

The measured PAL-filtered tungsten spectrum with a peak energy of 23 keV is shown to the left in Fig. 2.6 compared to the unfiltered spectrum, and the gain is shown to the right together with model predictions. Several parameters from these

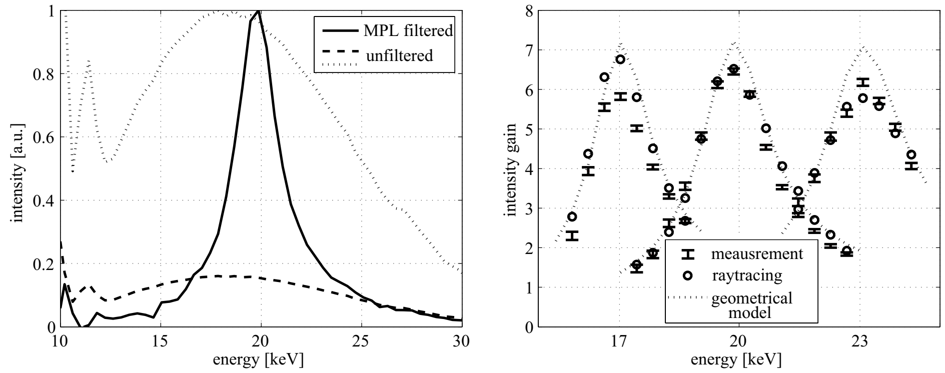

Figure 2.5: **Left:** Measured MPL-filtered and unfiltered spectra. **Right:** Intensity gain over a 10 μm slit for peak energies 17, 20, and 23 keV; measured, and predicted by the ray-tracing and geometrical models.

measurements and simulations are summarized in the middle part of Table 2.1. We see that the simple geometrical model agreed reasonably well with field-propagation and can be used for fast calculations. Experimental data showed almost perfect agreement with the field-propagation model in energy resolution and peak energy. The measured gain over a 14 μm slit, however, was 29% lower than predicted, which is attributable to a two times broader image.

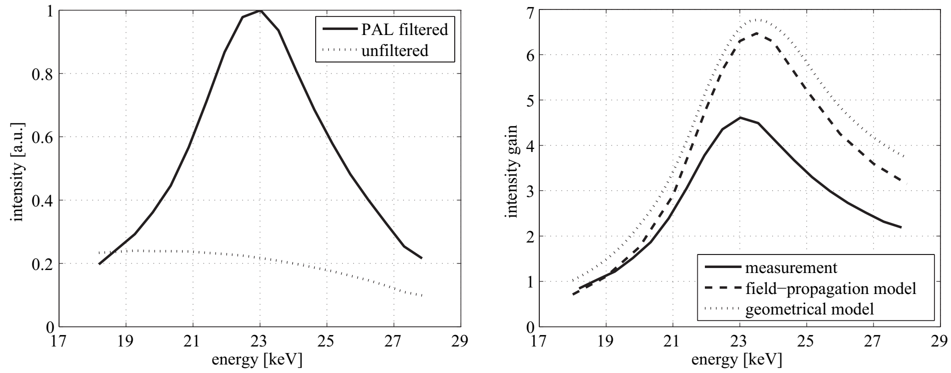

Figure 2.6: **Left:** Measured PAL-filtered and unfiltered spectra. **Right:** Measured intensity gain over a 14 μm slit compared to the field-propagation and geometrical models.

Results from the synchrotron measurements are summarized in the bottom part of Table 2.1. These measurements revealed that the broader image and reduced gain

Table 2.1: Parameters of the experimental lenses in bremsstrahlung and synchrotron setups at the peak energy (E_p). Simulations refer to ray tracing for the MPL and field propagation for the PAL. The gain (G) was calculated over 10 an 14 μm slits for the MPL and PAL respectively. Values of the focal length (F), source-to-lens and lens-to-image distances (s_o and s_i), physical aperture and transmission (D_p and t), source and image sizes (d_o and d_i), and energy resolution ($\Delta E/E_\mathrm{p}$) are given. The effective aperture is $D_\mathrm{e} = D_\mathrm{p} \times t$.

	F [mm]	E_p [keV]	$s_\mathrm{o}/s_\mathrm{i}$ [mm]	D_p [μm]	t	G	$d_\mathrm{o}/d_\mathrm{i}$ [μm]	$\Delta E/E_\mathrm{p}$
			Epoxy MPL, bremsstrahlung source					
measured	-	23.0	755/314	-	0.50	6.2	24/11	0.15
simulated	219	23.0	755/314	53	0.57	6.0	24/9.3	0.17
			Silicon PAL, bremsstrahlung source					
measured	-	23.0	585/296	194	-	4.6	25/18	0.29
simulated	178	23.5	585/296		0.35	6.5	25/8.9	0.29
			Silicon PAL, synchrotron source					
measured	-	23.0	40×10^3/225	194	-	2.1	270/14	-
simulated	178	23.0	185		0.33	2.6	6.8	-

was caused mainly by radiation from the peripheral part of the aperture (Fig. 2.7, Right), which is expected for phase distortions due to surface roughness according to Eq. (2.10). The deviation from model predictions of the measured peak intensity in the focal spot was 40% (Fig. 2.7, Left), which would correspond to $\sigma_\mathrm{t} = 350$ nm. We did not measure the surface roughness of the lens, but this figure is almost a factor of five higher than expected in the horizontal direction for an optimized etch process according to the lens manufacturer. Vertical roughness caused by the cyclic etch process can, however, be substantially larger, and even a very slight tilt of the lens would add to the phase error. Systematic over or under etch is also likely to have caused part of the deviation. A more thorough investigation of random and systematic phase errors, which was not regarded necessary for this particular study, would be to measure and include the deviations in the field-propagation model.

The experimental MPL and PAL cannot be directly compared because the PAL was made from a heavier material, and the measurement setup was shorter, which reduced the gain. Silicon was chosen as lens material because of readily available manufacturing methods and good-enough transmission for a proof-of-principle study, but as was noted above, an optimized lens is preferably manufactured in a polymer. On the other hand, the complexity of the PAL is higher than for the MPL, and it is likely that it will suffer more from manufacturing imperfections also

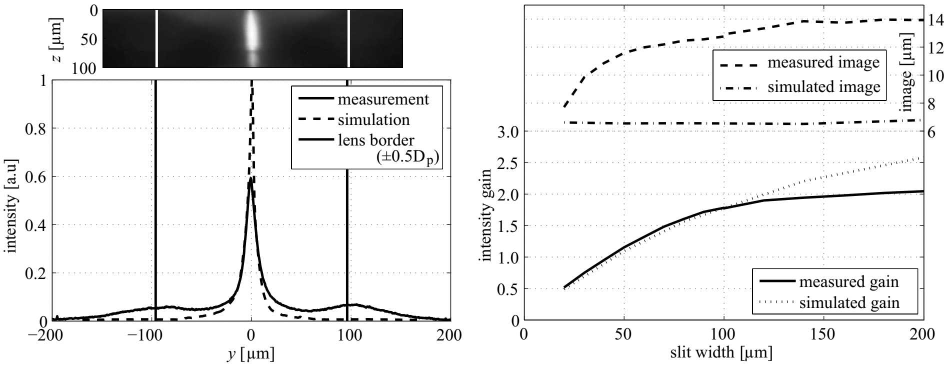

Figure 2.7: The synchrotron setup; measurements and simulations by the field-propagation model. **Left:** The measured intensity distribution in the focal plane is shown on top, with the focal line at the depth corresponding to the maximum intensity below. **Right:** The focal line width and the peak intensity gain over 14 μm as a function of an increasing collimator slit.

in the practical case. We can conclude that there is room for much improvement of the PAL by an optimized manufacturing process or a lens design with larger prism angles, whereas the experimental MPL was close to optimal.

Implementation in a clinical setup

Figure 2.8 (Left) shows typical spectra for the lens and reference systems at matching scan times. The SQE as a function of breast thickness is plotted in Fig. 2.8 and summarized in Table 2.2 for the lens systems with 25 and 100 μm sources, and for the reference system.

The MPL filter with focal length, peak energy, acceleration voltage, and aperture tuned to maximize the SQE for each breast thickness and source size reduced the dose compared to the reference system $13-16\%$ at matching scan times and an improved spatial resolution. Despite differences in the models, this result from Paper IV is in good agreement with Paper I, where a dose reduction of 14% was predicted. The improved spatial resolution of the MPL-filtered system is not necessarily desirable because the reference system may already be good enough, but it is not possible to trade resolution for SQE or flux because the aperture of the MPL is limited, and the larger source size had almost no effect on resolution. The PAL filter allows for larger apertures and both scan time and resolution could be matched to the reference system, resulting in a dose reduction of $20-24\%$, which was only $\sim 20\%$ higher than for the monochromatic case.

Also shown in Fig. 2.8 (Right) is the SQE for a fixed filter that was optimized at 50 mm breast thickness, and tuned only with the acceleration voltage. The

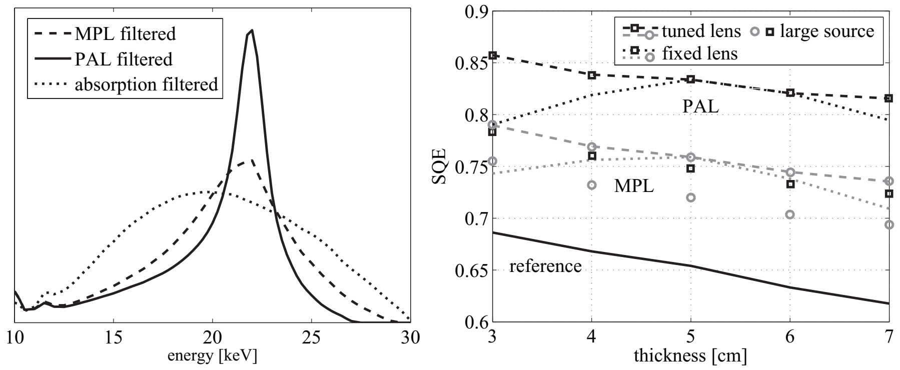

Figure 2.8: **Left:** Typical lens- and absorption-filtered spectra at matching scan times. **Right:** Spectral quantum efficiency (SQE) for the MPL (circles), PAL (squares), and reference (solid line) geometries. The lens filters with all parameters tuned in each point is shown for 25 and 100 μm sources (dashed line and no line), and the fixed filters that were optimized at 50 mm are shown for the 25 μm source (dotted line).

Table 2.2: Comparison of lens and reference systems in terms of spectral quantum efficiency (SQE) for breast thicknesses 30 – 70 mm. Dose reduction and scan time are relative the reference system. $\mathrm{MTF}_{0.5}$ is the spatial frequency at an MTF of 0.5.

	SQE	dose red. [%]	scan time	$\mathrm{MTF}_{0.5}$ [mm^{-1}]	source [μm]
MPL:	0.79 – 0.74	13 – 16	matched	6.3 – 6.6	25
	0.76 – 0.69	9 – 11		6.9 – 6.7	100
PAL:	0.86 – 0.82	20 – 24	matched	matched	25
	0.78 – 0.72	12 – 15			100
Abs.:	0.68 – 0.62	-	-	5.5	450

performance is only slightly degraded away from the optimum if the filter cannot be changed or tuned in practice. The benefit compared to the reference system decreased markedly when going to a larger source size, and it is evident that a thin line-shaped source is more or less required. It was concluded in Paper I, in accordance with others [102], that bright-enough micro-focal sources may already be feasible for medical imaging, and much development can be expected in this field [103]. The issue does, however, need further attention.

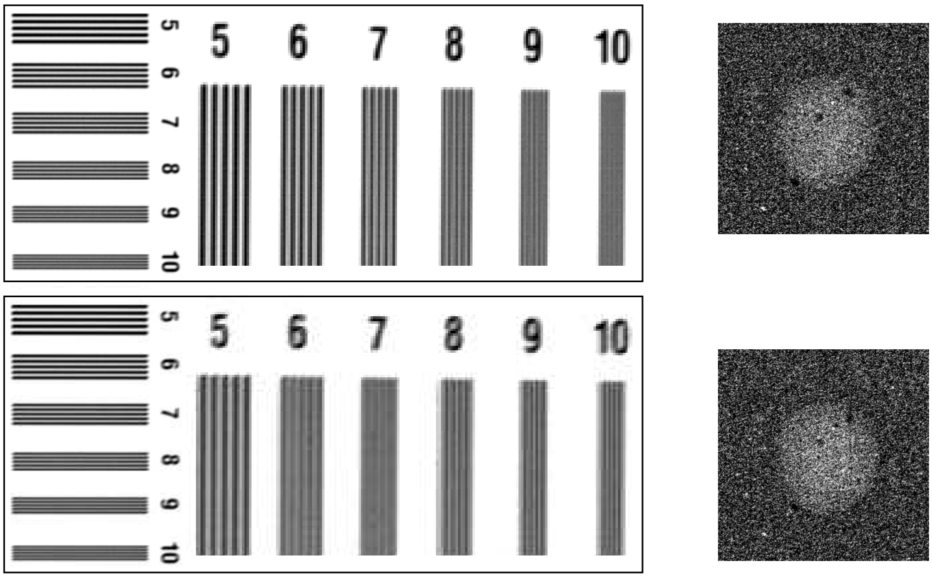

Figure 2.9: Images acquired with the MPL beam-focusing geometry (top), and the slit setup (bottom). **Left:** A bar-pattern phantom in the focusing (vertical lines), and nonfocusing direction (horizontal lines), at equal flux. **Right:** A 3 mm diameter low-contrast tumor in a tissue-equivalent phantom. The signal-to-noise ratios with the two setups are almost identical.

2.2.2 Beam focusing

The gain of flux of the MPL setup compared to a slit collimator at the same dose and better or equal MTF was measured to 1.32. Note that this gain is integrated over all energies and cannot be directly compared to the energy-dependent gain in the filtering setup. The gain in resolution was measured to ~ 1.4 at a similar flux. The latter is illustrated in Fig. 2.9 (Left), which shows images of a bar-pattern phantom acquired with the MPL and slit setups. The limiting resolution of the MPL setup appears to be at least 3 mm^{-1} higher in the focusing direction, whereas it is unaffected in the other direction. Figure 2.9 (Right) shows images of a 3 mm diameter artificial tumor in a 45 mm thick breast phantom for the MPL and slit setups at the same dose. The signal-to-noise ratios in these images are almost identical, which shows that there is no reduction in low-contrast performance due to *e.g.* scattering in the lens.

Figure 2.10 shows results from measurements and ray tracing, and summarizes several of the main conclusions of Paper II. A gain of flux is represented by a horizontal distance between the slit-collimator line and the MPL-collimator line. An optimized lens with no gap between the lens halves (diamond at (0,0) in Fig. 2.10)

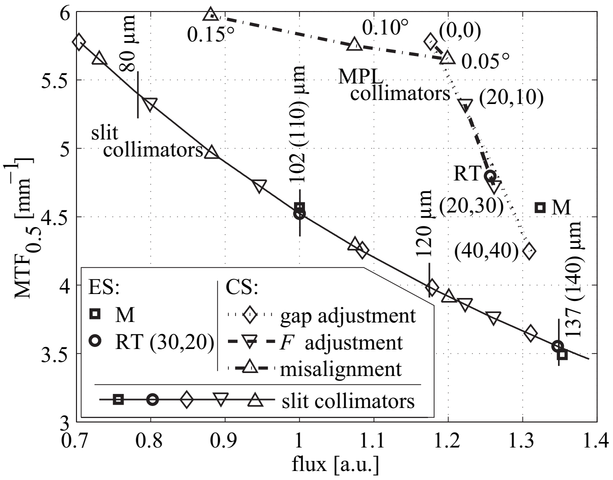

Figure 2.10: Spatial frequency at an MTF of 0.5 ($\mathrm{MTF}_{0.5}$) versus flux. This figure visualizes measurements (M) and ray-tracing (RT) results for the experimental setup (ES). In addition, ray-tracing results for a clinical setup (CS) are shown for adjustments in gap between the lens halves and focal length, and for a misaligned lens. Refer to Paper II for more details about this figure.

would yield a gain of flux of 1.67, or a gain in resolution of ~ 1.5 in a clinical setup. A misaligned lens reduced the transmission approximately 10% at a 0.1° displacement (standing triangle at 0.10°), which was not considered to be severe, and, in addition, the MTF was slightly improved. The flux-resolution relationship could be altered with the gap between the lens halves, but that reduced the overall efficiency of the collimator (diamonds and lying triangles).

Chapter 3

Spectral Imaging

3.1 Materials and Methods

3.1.1 Background

Phantom studies [24, 67–69] and clinical trials [66] have proven contrast-enhanced spectral imaging to be a promising approach for enhanced tumor detectability. Papers V and VI advance the technique further for the photon-counting detector in the multi-slit geometry.

Injection of contrast agent is probably not motivated for regular screening, and contrast-enhanced spectral imaging is expected to be an alternative mainly for diagnostic mammography at recalls. Enhancement of lesions without iodine uptake would be useful, since, in the case of electronic spectrum splitting, it comes as a bonus on top of the conventional image with no additional dose to the patient. Spectral imaging could potentially increase detectability of obscured lesions, and discriminate between solid and cystic lesions already in the screening image, for instance. Therefore, the framework presented in Paper VI was extended to include also imaging of tumors and microcalcifications without contrast agent, henceforth referred to as unenhanced imaging. Previous studies in this field have focused mainly on calcifications, predominantly with encouraging results [57–63], although some are more moderate [64]. The main difficulty appears to be that amplified quantum noise in the subtracted image may reduce detectability of small details. For tumor imaging, a few clinical investigations have been presented [54, 55]. There are also phantom studies that indicate feasibility for soft tissue imaging [24, 56], but the minimal attenuation difference between glandular and tumorous tissue, which is likely the main challenge [104], does not seem to be addressed.

3.1.2 Detector energy resolution

The detector that was used for measurements and simulations of spectral imaging is a prototype photon-counting detector, developed within the HighReX project and mounted on a Sectra MicroDose Mammography unit. Paper V provides an investigation of the detector energy response, which is a prerequisite to accurately model spectral imaging.

Figure 1.1 (Right) shows a schematic of the detector. A bias voltage is applied over the detector material, so that when a photon interacts, charge is released and drifts as electron-hole pairs towards the anode and cathode respectively. Each strip is wire bonded to a preamplifier and shaper, which are fast enough to allow for single photon-counting. The preamplifier and shaper collect the charge and convert it to a pulse with a height that is proportional to the charge and thus to the energy of the impinging photon. Pulses below a few keV are regarded as noise and are rejected by a low-energy threshold in a discriminator. All remaining pulses are sorted into two energy bins by an additional high-energy threshold, and registered by two counters. A preamplifier, shaper, and discriminator with counters are referred to as a channel, and all channels are implemented in an application specific integrated circuit (ASIC). Anti-coincidence (AC) logic in the ASIC detects double counting from charge sharing by a simultaneous detection in two adjacent channels, and the event is registered only once in the high-energy bin of the channel with the largest signal. Spatial resolution and image noise is thus improved, but all energy information of charge-shared photons is lost.

Measurements, simulations, and published data were used as input parameters to a cascaded detector model, which was validated by comparison to threshold scans (integral pulse-height spectra) over several input spectra. Using the model, the energy response of the detector assembly could be assessed on a system level without monochromatic radiation, and the impact of various detector parameters could be estimated.

3.1.3 Contrast-enhanced spectral imaging

Paper VI presents a framework to characterize the performance of the multi-slit system for spectral mammography. For task-specific system performance, we can define an ideal-observer detectability index [105]

$$d'^2 = 2\pi \int_{\mathrm{Ny}} \mathrm{GNEQ}(\omega) \times C^2 \times F^2(\omega) \times \omega \, \mathrm{d}\omega, \tag{3.1}$$

where $C = \Delta s/\overline{I}$ is the target-to-background contrast in the image for signal difference Δs and mean image signal per unit area $\overline{I}$, F is the signal template, which integrates to the area of the target for unit contrast, ω is the spatial frequency in the radial direction, and the integral is taken over the Nyqvist region. For simplicity, all parameters are assumed rotationally symmetric. GNEQ is the generalized noise-equivalent number of quanta that includes detector and anatomical noise according to Richard and Siewerdsen [105, 106]. It is a reasonable extension of the standard NEQ that measures the detector noise performance [107], because the dominant source of distraction for many imaging tasks in mammography is the variability of the anatomical background, which is referred to as anatomical or structured noise [8, 9]. For a quantum-limited system,

$$\mathrm{GNEQ}(\omega) = \frac{\overline{I}^2 T^2(\omega)}{S_\mathrm{Q}(\omega) + S_\mathrm{A}(\omega)}, \tag{3.2}$$

where T is the modulation transfer function (MTF) of the system, and S_Q and S_A are the power spectra (NPS) of quantum and anatomical noise respectively.

Two spectral optimization schemes that appear in the literature are energy weighting and dual-energy subtraction. Somewhat simplified, energy weighting ignores S_A and maximizes C^2/S_Q, whereas dual-energy subtraction instead minimizes S_A. S_A and S_Q can be expected to have completely different frequency distributions, and depending on the particular F, these two extremes are often good approximations. Paper VI, however, considers a general optimization of Eq. (3.1).

If the low- and high-energy images are normalized with the expected number of counts from mean breast tissue, a combined image with zero mean can be formed according to

$$I(x,y) = w\frac{n_{lo}(x,y)}{\overline{n}_{lo}} + \frac{n_{hi}(x,y)}{\overline{n}_{hi}} - (w+1) \approx w \ln\left[\frac{n_{lo}(x,y)}{\overline{n}_{lo}}\right] + \ln\left[\frac{n_{hi}(x,y)}{\overline{n}_{hi}}\right], \tag{3.3}$$

where w is a weight factor, and n_{hi} and n_{lo} are the high- and low-energy images. The logarithmic approximation is valid for $n \approx \overline{n}$, *i.e.* small signal differences. It is the usual expression for dual-energy subtraction, which is more suitable than the linear combination for reducing contrast between two materials because signals in I are proportional to target thickness. To estimate d', however, the linear combination was used so that signals in I are proportional to the number of quanta. Normalization with the expected number of counts in Eq. (3.3) is a detour to convey the derivations. A consequence is that Eq. (3.2) does not make sense because $\overline{I} = 0$, but the product $\mathrm{GNEQ} \times C^2$ is still valid, and the detectability index is not affected. In the practical case, a combination of the non-normalized images is more handy; *i.e.* $I' = w' n_{lo} + n_{hi}$, where $w' = \zeta_{hi}/\zeta_{lo} w$ (or the logarithmic counterpart with $w' = w$). A conventional non-energy-resolved absorption image is found for $I'(w' = 1)$, and the GNEQ without anatomical noise reduces to the standard NEQ.

The agent-to-background signal difference in the combined image is

$$\Delta s = |\overline{I} - I(d_\mathrm{c})| \approx d_\mathrm{c} |w \Delta\overline{\mu}_{\mathrm{cb},lo} + \Delta\overline{\mu}_{\mathrm{cb},hi}|, \tag{3.4}$$

where d_c is the integrated thickness of contrast agent, and $\Delta\overline{\mu}_{\mathrm{cb},\Omega} \equiv \overline{\mu}_{\mathrm{c},\Omega} - \overline{\mu}_{\mathrm{b},\Omega}$ is the difference in effective linear attenuation between the contrast agent and mean breast tissue for $\Omega \in \{lo, hi\}$, *i.e.* $\Delta\overline{\mu}_{\mathrm{cb},\Omega} \equiv \overline{\mu}_{\mathrm{c},\Omega} - \overline{\mu}_{\mathrm{b},\Omega}$. The approximation in Eq. (3.4) is valid for $\Delta\overline{\mu}_{\mathrm{cb},\Omega} \ll 1$. Further, if we assume no correlation between the energy bins, the quantum noise is

$$S_\mathrm{Q}(\omega) = \sum_\Omega \left[\frac{\partial I}{\partial n_\Omega}\right]^2_{\overline{n}_\Omega} \times S_{\mathrm{Q}\Omega}(\omega) \approx \frac{1}{q_0}\left[\frac{w^2}{\zeta_{lo}} + \frac{1}{\zeta_{hi}}\right], \tag{3.5}$$

where the approximation is for spatially uncorrelated noise. This result is in accordance with previous studies [105]. Anatomical noise in breast tissue has a relatively small deterministic component, and can be well described by an inverse power function [8]; $S_{\mathrm{A}g}(\omega) = \alpha(\overline{g})\omega^{-\beta}$. For the assumption that the shape of the NPS (*i.e.* β) is independent of x-ray imaging and image combination, except through filtering with the MTF, the anatomical noise in the image is

$$S_{\mathrm{A}}(\omega) \approx \left\langle \left[\frac{\mathrm{d}I}{\mathrm{d}g}\right]^2 \right\rangle S_{\mathrm{A}g}(\omega)T^2(\omega) \approx d_{\mathrm{b}}^2[w\Delta\overline{\mu}_{\mathrm{ag},lo} + \Delta\overline{\mu}_{\mathrm{ag},hi}]^2 S_{\mathrm{A}g}(\omega)T^2(\omega), \quad (3.6)$$

where $g(x,y)$ is the glandular fraction in the breast, d_{b} is the breast thickness, and $\Delta\overline{\mu}_{\mathrm{ag},\Omega}$ is the difference in effective linear attenuation between adipose and glandular tissue. The first approximation of Eq. (3.6) is for piecewise linearity of $I(g)$, whereas the second one assumes linearity across the range of glandularities and $\Delta\overline{\mu}_{\mathrm{ag},\Omega} \ll 1$. We note that S_{A} is independent of dose, as opposed to S_{Q}. Increasing the dose therefore does not improve the GNEQ if anatomical noise dominates, contrary to the standard NEQ. Maximization of $\Delta s^2/S_{\mathrm{Q}}$ and $1/S_{\mathrm{A}}$ yields the optima for energy weighting and dual-energy subtraction, respectively;

$$w^*_{s^2/S_{\mathrm{Q}}} = \zeta_{lo}\Delta\overline{\mu}_{\mathrm{bc},lo}/\zeta_{hi}\Delta\overline{\mu}_{\mathrm{bc},hi}, \quad \text{and} \quad w^*_{1/S_{\mathrm{A}}} = -\Delta\overline{\mu}_{\mathrm{ag},hi}/\Delta\overline{\mu}_{\mathrm{ag},lo}. \quad (3.7)$$

We note that the same weight factors have been reported previously for energy weighting [76], and dual-energy subtraction [78].

Paper VI presents a theoretical model of the spectral imaging system, based mainly on the detector model from Paper V and the derivations above. Several parts of the model were benchmarked to measurements on a phantom with oil-PMMA simulated anatomical clutter and $1-9$ mm deep containers with 5.7 mg/ml iodinated contrast agent. This relatively high concentration was used to avoid measurement uncertainties when comparing to the model. Images with 3 mg/ml iodine, which is a clinically feasible concentration for tumor uptake [108], were acquired for comparison. Eq. (3.1) was used as a figure of merit for optimization and for comparison to conventional absorption imaging.

3.1.4 * Unenhanced spectral imaging

The framework and model in Paper VI were extended for unenhanced imaging of tumors and microcalcifications. A prerequisite was that the spectral image should come as a bonus on top of an optimal absorption image, which limited the choice of incident spectra and dose range. On the other hand, since there is no K-edge in unenhanced imaging, the choice of split energy is free and can be chosen to minimize quantum noise. In addition, the sensitivity to a limited energy resolution can be expected to be lower because of no discontinuities in the spectrum.

No measurements were available, and images with anatomical noise were instead synthesized. The purpose of the images was twofold; to measure the noise in combined images for verification of Eqs. (3.5) and (3.6), and to visualize the result of image combination. A tungsten target x-ray tube with 0.5 mm aluminum filtration and 30 kVp acceleration voltage was assumed if not otherwise stated. The object was a 50 mm breast with 5 mm skin thickness and embedded lesions. It was imaged at a dose of 1 mGy, and quantum noise was added with a fraction double-counted photons calculated by the detector model. Glandular structure was generated using the clustered lumpy background technique [109]. The structure was chosen to range over all glandularities with a 50% glandularity mean. Published x-ray spectra [31], x-ray attenuation coefficients [32], and dose coefficients [33] were used as input. Tumor x-ray attenuation was gathered from Johns and Yaffe [104], and calcium phosphate ($Ca_3P_2O_8$) microcalcifications were assumed. Relatively large tumors of 20 mm diameter or more were assumed, which includes approximately 30% of all missed breast cancers [110].

System characterization

Two 1536×1536 pixel images (corresponding to $\sim 80\times80$ mm^2) were generated with respectively pure anatomical and pure quantum noise. The NPS was measured in absorption and combined images as a radial average in a similar way as described in Paper VI for the experimental phantom. A linear combination according to Eq. (3.3) was used for image combination.

S_A in the absorption image was fitted to the measured NPS in a region that was unaffected by window artifacts. The anatomical noise in combined images was then calculated using Eq. (3.6) and assuming a flat distribution of glandularities, although this likely overestimated the noise.

Quantum noise was calculated according to

$$S_{\mathrm{Q}\Omega}(u) = \overline{n}_\Omega \frac{1+\chi_\Omega[1+2\cos(2\pi u/p)]}{1+\chi_\Omega}, \tag{3.8}$$

where χ is the fraction double-counted events, p is the pixel size, and u is the spatial frequency in the detector direction [Paper V]. In the scan direction (spatial frequency v), $S_\mathrm{Q}(v)$ was assumed flat because readouts are uncorrelated. $S_\mathrm{Q}(\omega)$ in the absorption image was found as the radial average along the $u = v$ line, and $S_\mathrm{Q}(\omega)$ in combined images was calculated with Eq. (3.5). The latter is minimized for a bin count fraction

$$\xi_{lo} = 1 - \xi_{hi} = \frac{|w|}{1+|w|}, \tag{3.9}$$

which could determine a suitable split energy. If not otherwise stated, a count fraction close to 0.5 was, however, chosen in order to reduce complexity of the optimization.

As in Paper VI, the MTF was assumed equal in both energy bins, although double counting degraded the resolution somewhat in the high-energy bin, which generally affects the GNEQ [111]. In addition, the MTF was assumed radially symmetric in the calculations with $T(\omega)$ equal to the mean of the axial MTFs, although this scheme does not in general represent the two-dimensional MTF correctly [112].

These simplifications were regarded justified because the difference in MTF between the bins was small, and the major differences between optimally combined images and conventional absorption images are in the region where anatomical noise dominates, *i.e.* at low spatial frequencies where $T(\omega) \approx T_{lo}(\omega) \approx T_{hi}(\omega) \approx T(0) = 1$.

For tumors, a Fourier transform of the designer nodule function with $v = 1.5$ was used as signal template [8, Paper VI], and microcalcifications were assumed spherical. The signal difference was calculated according to Eq. (3.4), and the detectability index could be found from Eq. (3.1).

Images for visualization

For visualization of the optimal image combination, images with both quantum and anatomical noise were generated, and tumors with a profile according to the designer nodule function were inserted. Additional lumps of pure glandular tissue, with the same profile and attenuation as the tumors, simulated cysts. The images were filtered with the MTF.

Instead of the linear image combination that was used for system characterization, a polynomial-weighted logarithmic subtraction was introduced to gain better background subtraction than with a constant weight factor, *i.e.* $w = w(n_{lo}, n_{hi})$ in Eq. (3.3). The polynomial was trimmed to minimize the variance of a phantom with seven levels of glandularity. A second degree polynomial was found to provide a good-enough minimization. It can be noted that similar nonlinear techniques are employed for material-basis decomposition [38, 57]. More efficient optimization schemes could be conceived, *e.g.* maximization of C^2/S_{A}.

Simulated images were low-pass filtered to reduce quantum noise. Equal filters were applied to both bins prior to forming the combined image, which is reasonable if the bin count fraction is close to 50%. More advanced filtering methods have been shown to improve detectability considerably [57, 111], and also to influence the optimization because unequal filtering of the bins does not cancel in the GNEQ.

3.2 Results and Discussion

3.2.1 Detector energy resolution

Scans of the high-energy threshold over several different spectra are shown in Fig. 3.1 (Left) together with the fitted model. Overlaid on the plot is the relationship between threshold level and photon energy, which is nonlinear. The energy resolution of the experimental detector was found to be $\Delta E/E = 0.12 - 0.26$ in the relevant energy range, as is illustrated in Fig. 3.1 (Right). The major factors contributing to the width of the response function were electronic noise, followed by charge sharing, and a channel-to-channel threshold spread that was boosted by the nonlinear relationship between threshold and energy. Additionally, a relatively large constant background of charge-shared photons detected by the AC logic was added to the high-energy bin. The shaper dead time and AC time window were

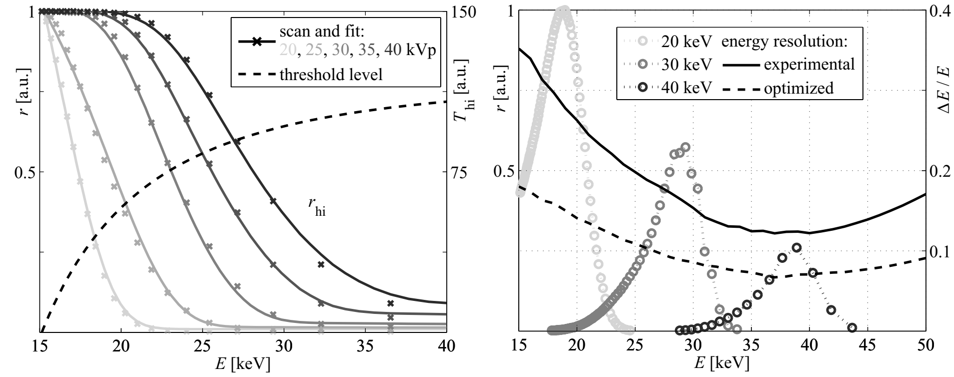

Figure 3.1: **Left:** Scans of the high-energy threshold over 20 – 40 kVp spectra. The high-energy threshold level as a function of energy is shown as a dashed line. **Right:** Energy response to monochromatic delta peaks, and the energy resolution ($\Delta E/E$) for the experimental detector, and for an improved detector.

both less than 200 ns, and pile-up and chance coincidence were found to be of minor importance at mammography count-rates. Fluorescence and scattering effects in the silicon were estimated to be negligible.

Figure 3.1 (Right) also shows the energy resolution of an improved detector with high AC efficiency and low threshold spread and electronic noise. Relatively large improvements of the energy resolution are within reach. Minimization of the electronic noise is highly important to reduce the peak broadening. The trimming point should be chosen close to the point of operation of the threshold, and variations between channels should be kept at a minimum in order to minimize the threshold spread. This is primarily important for the high-energy threshold, which is meant to operate in high-intensity parts of the spectrum. An improvement in shaper and discriminator linearity at higher energies is also desirable to reduce the effects of threshold spread and limited bit depth. Finally, the AC scheme can be improved by keeping the energy resolution of detected events, or by recording them in a separate bin.

3.2.2 Contrast-enhanced spectral imaging

Detectability index as a function of weight factor is plotted in Fig. 3.2. Note that positive weight factors are normalized so that a conventional absorption image is located at $w' = \zeta_{hi}/\zeta_{lo}w = 1$, which is the reason for the dent at $w = w' = 0$. It is clear that in this case, with a substantial amount of anatomical noise and a target contrast that is very different from breast tissue, the optimal image combination is minimization of S_{A}, which corresponds to the dual-energy subtraction scheme. For imaging of iodine, the optimal weight factor predicted by Eq. (3.7) for energy weighting was less than unity because of higher target attenuation in the high-energy bin. The predicted weight factor missed the local maximum for energy weighting, which is due to inclusion of anatomical noise, but the improvement over absorption imaging even at the maximum was only in the order of 1%. The global minimum corresponds to minimization of the iodine contrast.

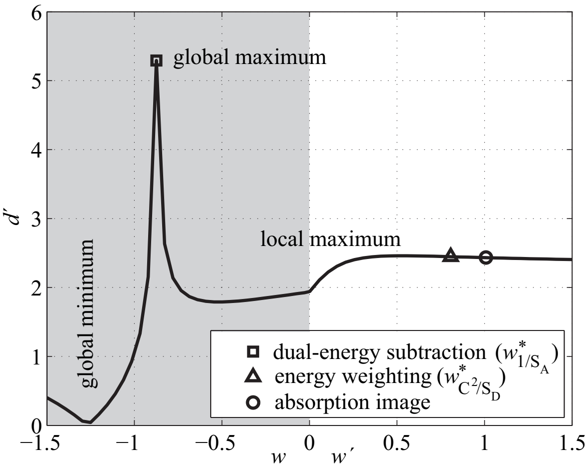

Figure 3.2: Detectability index (d') as a function of weight factor for the phantom. Positive weight factors are normalized so that a conventional absorption image is located at $w' = 1$.

Figure 3.3 shows images of the phantom, acquired with a dose that corresponds to an AGD of 0.94 mGy. On the top row is an image of the contrast phantom without clutter, which shows the locations of the iodine containers. The subsequent two rows are images for iodine concentrations of 6 and 3 mg/ml. To the left are non-energy-resolved absorption images of the phantom with clutter that hid the containers. The right-hand images are optimally combined according to Fig. 3.2, which efficiently removed the clutter. At least eight 5.7 mg/ml containers (down to 2 mm, *i.e.* an area concentration of 1.1 mg/cm^2) were visible. The contrast-to-noise ratio in the 3 mg/ml image was substantially lower, but five to seven containers were still distinguishable.

A logarithmic plot of the quantum and anatomical NPS in the absorption and optimally combined images is shown in Fig. 3.4. In the absorption image, anatomical noise clearly dominated at low spatial frequencies, but was reduced almost six orders of magnitude in the combined image for a similar quantum noise. Target contrast was, however, also reduced in the combined image. This is further illustrated in Fig. 3.5, which shows the different parts of Eq. (3.1); GNEQ multiplied with the contrast squared (GNEQ × C^2), and the task function squared multiplied with the spatial frequency ($F^2 \times \omega$). The combination of these two plots gives an

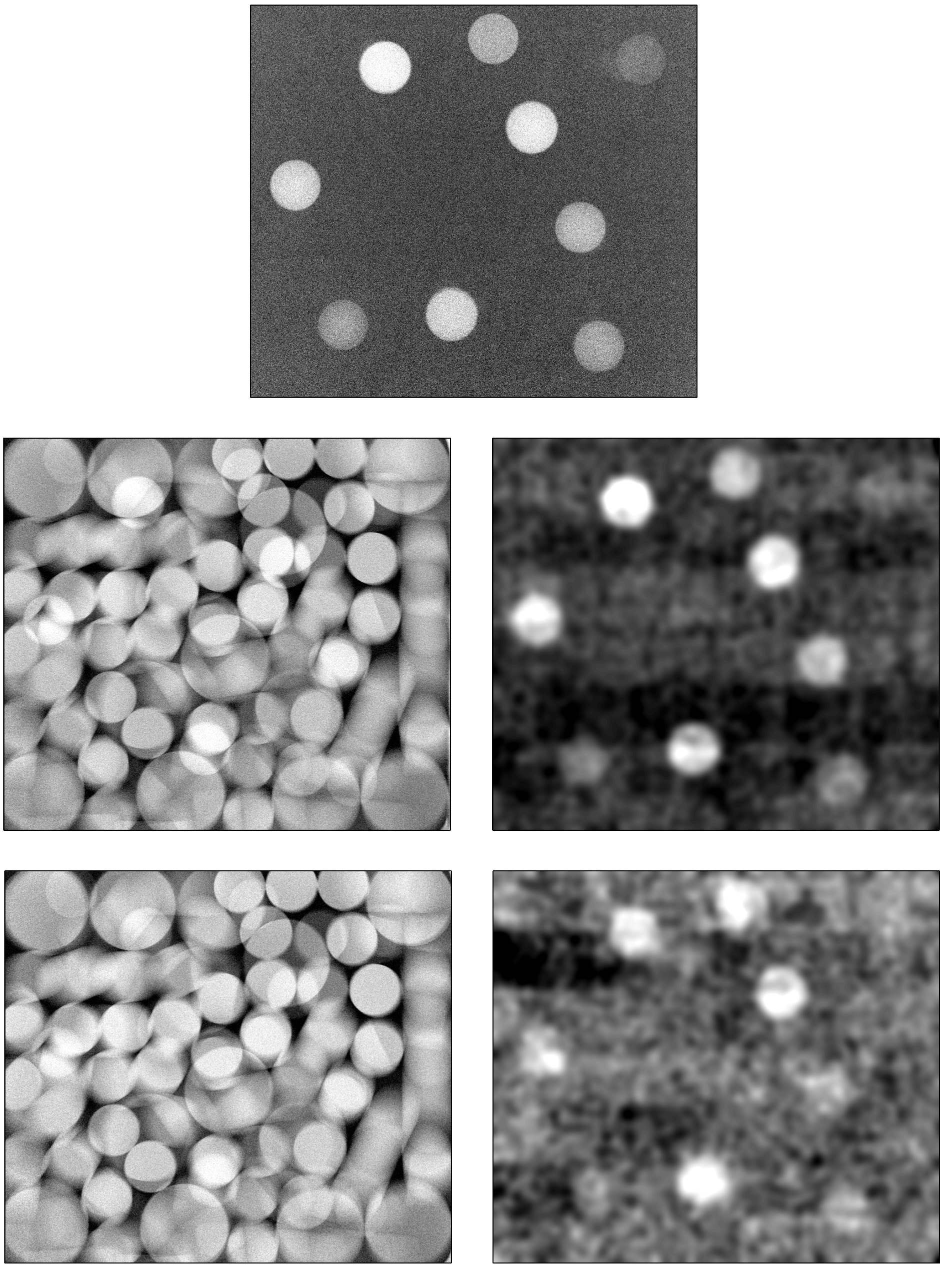

Figure 3.3: Images of the phantom at an AGD of 0.94 mGy. **Top:** Absorption image without clutter. **Center:** 6 mg/ml iodine: Absorption image with clutter (Left), and optimally combined image with the clutter removed (Right). **Bottom:** Ditto for 3 mg/ml iodine.

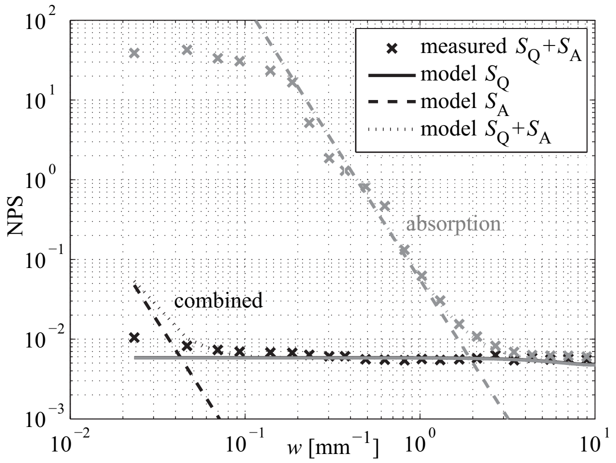

Figure 3.4: Logarithmic plot of quantum and anatomical NPS ($S_{\mathrm{Q}}(\omega)$ and $S_{\mathrm{A}}(\omega)$) for absorption and combined images of the phantom. Crosses indicate measurements directly in the phantom images, and lines show fits to measurements or model predictions.

indication of the detectability index for absorption and combined images. It is evident that GNEQ $\times\, C^2$ of the combined image was inferior to the absorption image at high spatial frequencies, but was optimized for low frequencies ($\omega < 1$ mm^{-1}), where $F^2 \times \omega$ has most of its frequency components.

The first two rows of Table 3.1 show d' calculated for the 5 mm container in the optimally combined image (Fig. 3.3 (Right), and the square marker in Fig. 3.2), and for the absorption image (Fig. 3.3 (Left), and the circle in Fig. 3.2). Detectability was increased by more than a factor of 2, which seems reasonable for a subjective comparison to Fig. 3.3, and gives some validation to the model and d' as a figure of merit.

The next group of rows concern simulation results for a contrast-enhanced tumor embedded in average or dense breast tissue, imaged at an AGD of 0.94 mGy. Average tissue was assumed to have a glandularity of 0.5, and an anatomical noise level so that S_{A} crossed S_{Q} at 1 mm^{-1}. Dense tissue was assumed to have a glandularity of 0.8 and an S_{A}-S_{Q} crossing at 2 mm^{-1}. The result for the current experimental setup is shown in row 3, and the subsequent rows illustrate relatively straightforward system improvements; 45 – 50 kV acceleration voltage (rows 4 – 5), optimized detector performance (row 6), and a combination of both (row 7). Results for a conventional absorption image are shown in row 8. We note that for combined images, the difference in detectability between average and dense breast tissue was small, as opposed to the conventional absorption images. Hence, al-

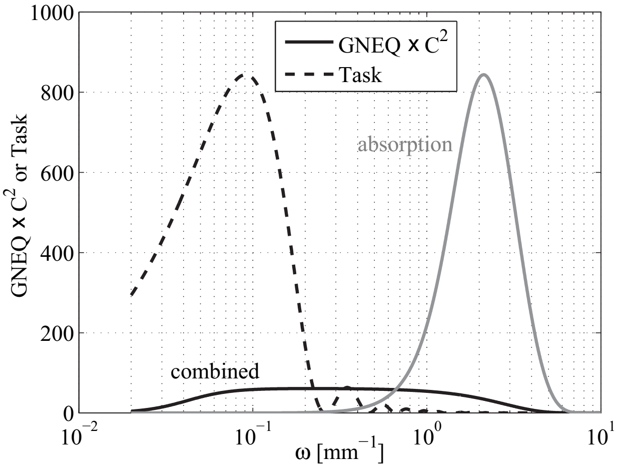

Figure 3.5: Generalized NEQ times contrast squared ($\mathrm{GNEQ}(\omega) \times C^2$) for absorption and combined images of the phantom with the task function ($F^2(\omega) \times \omega$) superimposed to illustrate the effect of integration to detectability index in Eq. (3.1).

ready the experimental setup can be expected to improve detectability compared to absorption imaging close to 80% in average breast tissue, but almost a factor of 8 for a dense breast, and this is where spectral imaging can be expected to be most beneficial. There is much room for system optimization, and a combination of an optimized detector and 45 kV acceleration voltage improved the result $\sim 70\%$ compared to the experimental setup.

3.2.3 * Unenhanced spectral imaging

Synthesized images at 1 mGy of three 20 mm thick tumors with diameters 20, 30, and 40 mm embedded in a 50 mm breast are shown in Fig. 3.6. The top image shows the tumors, which are hidden by anatomical and quantum noise in the left image. In addition, two cysts with equal size and attenuation as the tumors were added in the center and in the lower-left corner of the image. The polynomially combined image is shown to the right with all tumors visible and all false positives excluded. Anatomical noise was reduced at the cost of a lower tumor contrast, and quantum noise dominated in the combined image. Low-pass filtering with a 1.5 mm Gaussian kernel was therefore applied. It should be noted that filtering of the absorption image would reduce high-frequency noise, but not exclude the false positives. In addition, a narrow display window helped visualize the tumors in the combined image, but would not improve the absorption image. Smaller and thinner tumors than the ones imaged here were found hard to visualize because of quantum noise dominance and reduced contrast respectively.

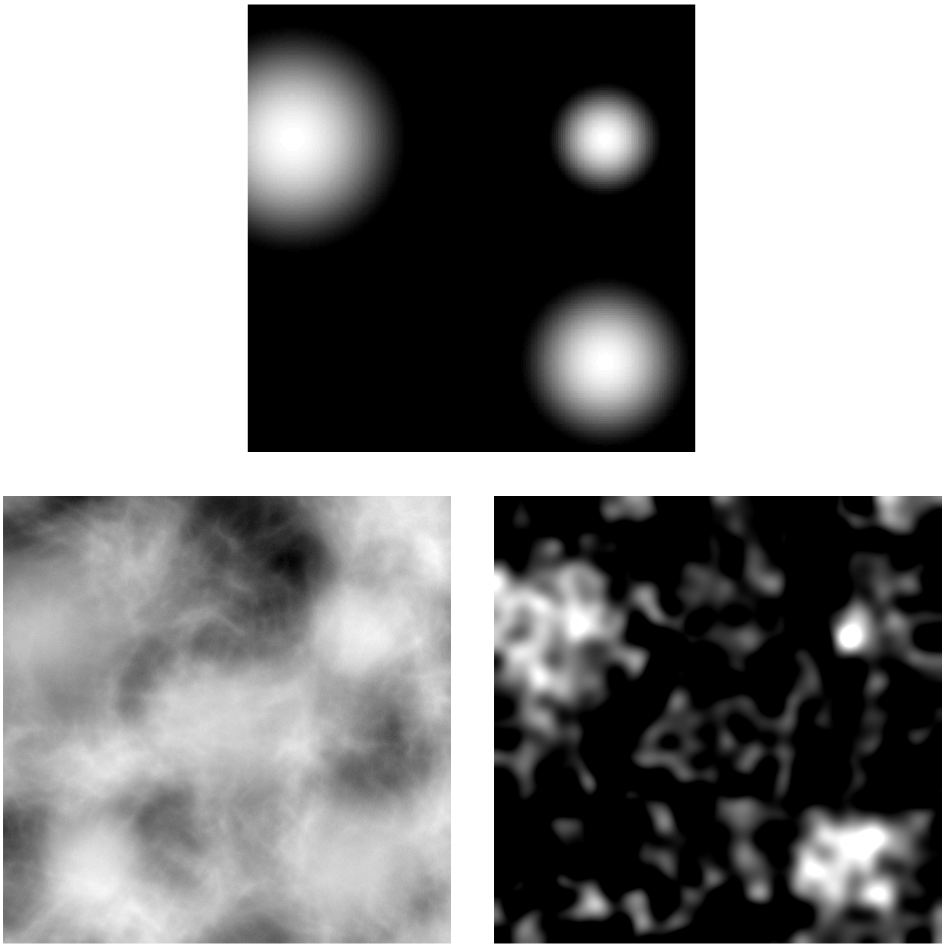

Figure 3.6: Synthetic images of three 20 mm thick tumors with diameters 20, 30, and 40 mm at an AGD of 1.0 mGy. **Top:** Tumor locations. **Left:** Absorption image with synthesized anatomical noise. **Right:** Optimally combined image, where all tumors are visible and all false positives are excluded.

Table 3.1: Detectability index for the experiment, simulations of contrast-enhanced tumors in average or dense breast tissue, and simulations of unenhanced tumors and microcalcifications. Results are for optimally combined (comb.) and absorption (abs.) images. Optimization is done with acceleration voltage (kV), and the experimental compared to an optimized detector.

image	detector	kV	Al filter [mm]	detectability	
contrast enhanced:			experiment, 5 mm container, 5.7 mg/ml iodine		
comb.	experim.	40	3.0		**41**
abs.	experim.	40	3.0		**19**
simulation, 5 mm tumor, 3 mg/ml iodine,				average tissue,	dense tissue
comb.	experim.	40	3.0	**5.3**	**5.1**
comb..	experim.	45	3.0	**6.3**	**6.0**
comb.	experim.	50	3.0	**6.5**	**6.0**
comb.	opt.	40	3.0	**8.1**	**7.6**
comb.	opt.	45	3.0	**9.4**	**8.4**
abs.	opt.	28	0.5	**3.0**	**0.66**
unenhanced:			simulation,	20 mm tumor,	0.4 mm MC
comb.	experim.	30	0.5	**22**	**0.00271**
comb..	experim.	40	0.5	**21**	**0.00262**
comb.	opt.	30	0.5	**22**	**0.00270**
abs.	opt.	30	0.5	**14**	**0.00268**

A logarithmic plot of the quantum and anatomical NPS in an absorption image and an image combined for maximum background subtraction is shown in Fig. 3.7. S_{A} measured in the synthesized image crossed S_{Q} at $\omega = 2.3\ \mathrm{mm}^{-1}$ with an exponent $\beta = 3.1$. The latter is indeed reasonable for breast tissue; β values between three and four have been published [8, 109, 113]. The magnitude, on the other hand, was difficult to validate. Burgess reported that the anatomical noise in digitized mammograms dominated below $\sim 1\ \mathrm{mm}^{-1}$ [8], which indicates that the noise magnitude in the simulated images was higher than average but not totally arbitrary. A measurement of the NPS in clinical images with the multi-slit system would be required to fully settle this issue.

Optimal combination with a constant weight factor reduced the quantum noise slightly, and reduced the anatomical noise approximately three orders of magnitude. A polynomial weight factor reduced the anatomical noise another four orders of magnitude at equal quantum noise. Nevertheless, the following derivation of detectability index was based on the linear combination in Eq. (3.3) to ensure linearity, although the polynomial combination can be expected to perform better. S_{Q} cal-

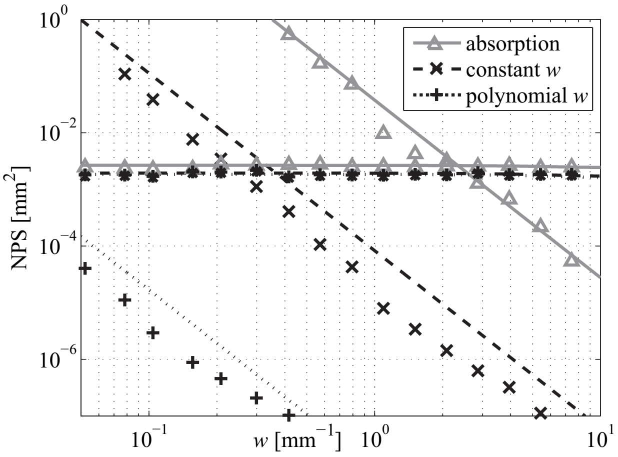

Figure 3.7: Logarithmic plot of quantum and anatomical NPS in synthesized absorption and combined images. Markers indicate measurements, and lines show fits to measurements or model predictions.

culated by Eq. (3.5) corresponded well to measurements in the synthesized images. Equation (3.6) assumes that β is independent of image combination, which is clearly an approximation, and dependency on weight factor has in fact been reported previously [114]. Nevertheless, the assumption of a flat glandularity distribution lead to a slight overestimation of the NPS magnitude in the combined image, which dominated over the change in β. Model predictions based on Eq. (3.6) therefore are expected to be moderate, and can be used with confidence. It should be kept in mind, however, that Eq. (3.6) only gives an indication of the noise and not the exact level.

Detectability index as a function of weight factor is plotted in Fig. 3.8 normalized to the absorption image, and for three different cases; (1) a 20 mm tumor in anatomical and quantum noise (similar to Fig. 3.6), (2) a 400 μm microcalcification in anatomical and quantum noise, and (3) a tumor on a flat background with only quantum noise. Again, positive weight factors were normalized so that an absorption image is located at $w = 1$, but ζ_{hi}/ζ_{lo} was close to unity so there was no dent at $w = 0$. For the tumor in anatomical noise, optimal combination was found to be close, but clearly not identical, to dual-energy subtraction. Energy weighting according to Eq. (3.7) was suboptimal because higher weighting of the low-energy photons also increased the anatomical noise, and, in fact, excluding the low-energy image altogether ($w = 0$) resulted in the highest detectability. For the small microcalcification, however, dual-energy subtraction was suboptimal, whereas energy weighting provided a minute improvement. A similar result was found for the tumor on uniform background, and the optimal weight factors for these targets

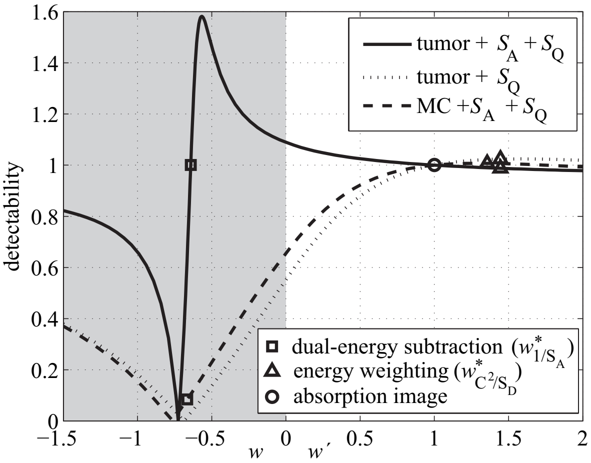

Figure 3.8: Detectability as a function of weight factor normalized so that a conventional absorption image is located at (1,1). Three cases are considered; a 20 mm tumor in anatomical and quantum noise ($S_\mathrm{A} + S_\mathrm{Q}$), the tumor on a homogenous background, and a microcalcification with both types of noise.

almost coincided. The optimal energy thus seems fairly independent of lesion type, which is in accordance with previous studies [36, 101].

Figure 3.9 shows the different parts of Eq. (3.1) at optimal image combination for the unenhanced tumor in anatomical noise. Compared to Fig. 3.5, the tumor contrast of the combined image was substantially lower, and benefit relative the absorption image was found only at frequencies below $\sim 0.5\ \mathrm{mm}^{-1}$, where, however, the tumor task function was located. The microcalcification task function, on the other hand, increased with spatial frequency due to the two-dimensional integration, and is hence virtually unaffected by the anatomical noise; dual-energy subtraction was therefore suboptimal.

A split energy of 21 keV provided a bin count fraction of approximately 0.5, and was used for all of the above cases. A scan of split energies at the optimal weight factor for tumor imaging (-0.57) revealed that the optimum for this case was 18.5 keV, which, however, improved the detectability less than 1%, and the spectrum can hence be safely split at the center. It can be noted that 18.5 keV yields $\xi_{lo} = 0.33$, which is close to 0.36 as predicted by Eq. (3.9).

The last group of rows of Table 3.1 concern detectability for optimally combined images in the unenhanced case with an absorption image on the bottom row. Detectability of the tumor can be improved 57% by optimal combination, which seems reasonable when comparing to Fig. 3.6. Optimal combination for imaging the microcalcification yielded an improvement in the order of 1%, which is clearly not worth the effort. Neither beam quality nor improved detector performance was

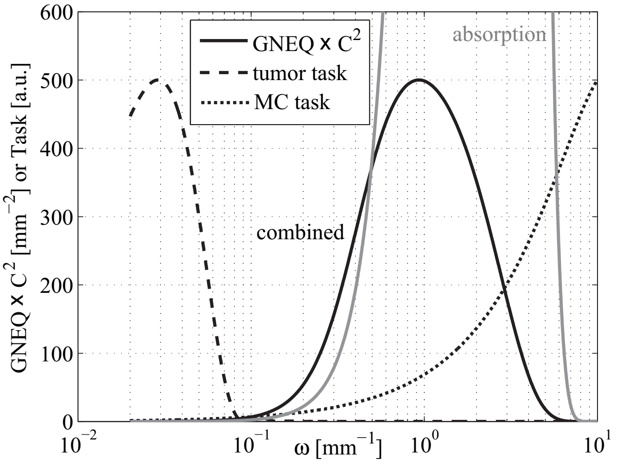

Figure 3.9: Generalized NEQ times contrast squared (GNEQ(ω) $\times$ C^2) with the task functions ($F^2(\omega) \times \omega$) for a 20 mm tumor and a 400 μm microcalcification (MC).

found to influence the result materially. Note that the detectability in Table 3.1 varies with object size, and different targets are not directly comparable.

Some uncertainties in the model can be identified, including the magnitude of the anatomical noise, agreement between the model and real observers, and factors other than random noise, such as variations in thickness or anatomy, which might dominate in the practical case. Observer studies in realistic anatomical backgrounds [8, 106, 115] and clinical studies [66] are needed to fully investigate these effects. There are also several potential improvements to the technology, which warrant further study. These include optimization of spatial filtering for noise reduction [111], optimization of incident spectrum [24, 116], and nonlinear image combination [37, 38, 57, 73].

Chapter 4

Conclusions and Outlook

4.1 X-Ray Optics in Mammography

Two types of refractive x-ray lenses were investigated – the MPL and the PAL. A geometrical model and a ray-tracing framework were developed for the MPL, and shown to agree well with measurements on an epoxy lens. A geometrical model was also developed for the PAL, and field propagation was used to account for diffractive effects. These models were in reasonable agreement with measurements on a silicon lens, and discrepancies could be explained by the relatively large degree of lens imperfections.

Using the models to optimize performance, it was shown that filters based on the lenses can reduce dose in mammography. The dose of an MPL-filtered system was about 15% below that of an absorption-filtered reference system at matching signal-to-noise ratios and scan times, and the spatial resolution was higher. The dose of the PAL-filtered system was about 20% lower than that of the reference system when also the resolution was matched, and only about 20% higher than that of a monochromatic beam. The PAL clearly has greater potential for energy filtering than does the MPL, but the complexity is greater, and the MPL probably can be better optimized in actual applications. Investigating the feasibility of brilliant-enough x-ray sources and manufacturing of a polymer PAL remains.

Beam focusing is an application of x-ray optics that may be smoother to implement than spectral shaping in the existing multi-slit geometry because a smaller source is not needed. In fact, the existing pre-collimator could simply be exchanged for the lens array, and the gain comes in addition to any source developments that can be expected in the future. An epoxy lens was used to evaluate beam focusing experimentally, and a ray-tracing model was used to predict clinical performance. The gain in resolution or flux for the experimental lens in an optimized setup was found to be approximately 50%. Optimizing the lens design and implementing a PAL are areas of future research that may lead to further improvements.

4.2 Spectral Imaging

A cascaded model of the silicon strip detector was developed and validated with measurements. The merits of the model include that the energy response of the detector assembly can be assessed on a systems level without monochromatic radiation; the impact of various parameters on energy resolution can be estimated, which is crucial for system optimization; and spectral imaging with the system can be simulated.

Contrast-enhanced imaging was shown, experimentally and with simulations, to be beneficial compared to conventional absorption imaging for detecting tumors. The technique improved an ideal-observer detectability index by a factor of 2 to 8 for relatively small tumors at different levels of anatomical noise and breast density. Because of anatomical noise dominance, the same detectability cannot be reached by increasing the dose in an absorption image. The current experimental system is already feasible, but relatively straightforward upgrades of detector and beam quality may further improve performance by a factor of almost two. In conclusion, the potential of contrast-enhanced spectral imaging can be regarded as established from a technical standpoint, and it is a promising alternative to ultrasonography and MRI in diagnostic mammography.

Unenhanced spectral imaging has great potential because it comes as a bonus to the conventional absorption image at screening; there is no additional radiation dose to the patient and no need to inject contrast medium. Initial simulations indicated about a 50% improvement in detectability over absorption imaging for large tumors obscured by anatomical structures. These results are clearly encouraging, although they should be verified by experiment before drawing final conclusions. The performance was largely independent of beam quality, detector energy resolution, and bin count fraction, which simplifies optimization in the practical case. Several potential improvements to the image combination warrant further study, including spatial filtering and nonlinear combination.

For imaging contrast-enhanced tumors in the presence of anatomical noise, the optimal combination of the energy-resolved images corresponded exactly to maximal reduction of the anatomical noise, *i.e.* the dual-energy subtraction scheme. Higher weighting of the more-information-dense photons, referred to as energy weighting, yielded only a slight improvement compared to an absorption image. Imaging of large unenhanced tumors in the presence of anatomical noise corresponded closely, but not exactly, to dual-energy subtraction, and energy weighting deteriorated detectability. For small microcalcifications, or tumors on uniform backgrounds, the situation was reversed; dual-energy subtraction was clearly suboptimal whereas energy weighting provided a small benefit. Hence, the optimal image combination and benefit of spectral imaging depends to a large extent on the imaging task. Also including the anatomical noise in the analysis may yield completely different results than if the quantum noise alone is considered, which is common practice.

Finally, the detector model and framework that have been presented can be extended to future applications of the multi-slit system, in particular spectral tomosynthesis [117, 118].

Acknowledgements

A special thanks goes to my advisors Mats Danielsson and Björn Cederström. Mats for the encouragement, never ending stream of ideas, and for reminding me of the larger picture. Björn for sharing expert knowledge in all fields of science, for always coming up with solutions on tricky problems, and for going into the details. I am grateful to all colleagues and co-authors; Magnus Åslund for ideas and guidance; Peter Nillius for teaching me elementary mathematics; Carolina Ribbing for all the comments; Hans Bornefalk for keeping his feet on solid ground; Staffan Karlsson for not keeping his feet on solid ground; Cheng Xu for endless simulations; Mats Lundqvist and Magnus Hemmendorff for much help and rewarding discussions; Sandra Tibbelin, Lilián del Risco Norrlid, Kristina Juhlin, and all former members of the Medical Imaging group for keeping up the good spirit. All members of the Particle Physics group are kindly acknowledged for the great working atmosphere during the earlier parts of this work. I would also like to express my gratitude to the BIOX group for lending us their best and more or less irreplaceable test pattern, and for not being too upset when we broke it.

Many thanks to my extended family, Sune, Katarina, and Åsa, for believing in me and for being so proud. Finally, my wife Jennie and my son Hannes: Thank you for being there, for the effort during the last few months, and for the support. All this would have been pointless without you.

Bibliography

[1] *Cancer Incidence in Sweden 2007*. Socialstyrelsen (The National Board of Health and Welfare), 2008.

[2] P. Boyle and J. Ferlay. Cancer incidence and mortality in europe, 2004. *Ann. Oncol.*, 16(3):481–488, 2005.

[3] M. J. Horner, L. A. G. Ries, M. Krapcho, N. Neyman, R. Aminou, N. Howlader, S. F. Altekruse, E. J. Feuer, L. Huang, A. Mariotto, B. A. Miller, D. R. Lewis, M. P. Eisner, D. G. Stinchcomb, and B. K. Edwards, editors. *SEER Cancer Statistics Review, 1975-2006*. National Cancer Institute, Bethesda, MD, 2009.

[4] U. Veronesi, P. Boyle, A. Goldhirsch, R. Orecchia, and G. Viale. Breast cancer. *Lancet*, 365(9472):1727–1241, 2005.

[5] S. Shapiro, P. Strax, and L. Venet. Periodic breast cancer screening in reducing mortality from breast cancer. *JAMA*, 215(11):1777–1785, 1971.

[6] L. Tabár, B. Vitak, H. T. Chen, M. F. Yen, S. W. Duffy, and R. A. Smith. Beyond randomized controlled trials: Organized mammographic screening substantially reduces breast carcinoma mortality. *Cancer*, 91(9):1724–1731, 2001.

[7] M. J. Yaffe. *Handbook of Medical Imaging*, volume 1. Physics and Psychophysics, chapter 5. Digital Mammography. SPIE Press, Bellingham, USA, 2000.

[8] A. E. Burgess, F. L. Jacobson, and P. F. Judy. Human observer detection experiments with mammograms and power-law noise. *Med. Phys.*, 28(4): 419–437, 2001.

[9] F.O. Bochud, J.F. Valley, F.R. Verdun, C. Hessler, and P. Schnyder. Estimation of the noisy component of anatomical backgrounds. *Med. Phys.*, 26(7): 1365–1370, 1999.

[10] *Health Risks from Exposure to Low Levels of Ionizing Radiation: BEIR VII – Phase 2*. National Academies Press, Washington, DC, 2005.

[11] International Commission on Radiological Protection. Lowdose extrapolation of radiation-related cancer risk. In *Publication 99*, volume 35 of *Ann ICRP*. Elsevier, Oxford, 2006.

[12] J. Law J, K. Faulkner, and K. C. Young. Risk factors for induction of breast cancer by x-rays and their implications for breast screening. *Br. J. Radiol.*, 80:261–266, 2007.

[13] A. Karellas and S. Vedantham. Breast cancer imaging: A perspective for the next decade. *Med. Phys.*, 35(11):4878–4897, 2008.

[14] E. D. Pisano, C. Gatsonis, E. Hendrick, M. Yaffe, J. K. Baum, S. Acharyya, E. F. Conant, L. L. Fajardo, L. Bassett, C. D'Orsi, R. Jong, and M. Rebner. Diagnostic performance of digital versus film mammography for breast-cancer screening. *N. Engl. J. Med.*, 353(17):1773–1783, 2005.

[15] FDA, Center for Devices and Radiological Health, MQSA National Statistics. http:// www.fda.gov/ Radiation-EmittingProducts/ MammographyQuality-StandardsActandProgram/ FacilityScorecard/, October 2009.

[16] E. D. Pisano and M. J. Yaffe. Digital mammography. *Radiology*, 234(2): 353–62, 2005.

[17] M. Lundqvist, B. Cederström, V. Chmill, M. Danielsson, and D. Nygren. Computer simulations and performance measurements on a silicon strip detector for edge-on imaging. *IEEE Trans. Nucl. Science*, 47(4):1487–1492, 2000.

[18] M. Lundqvist, B. Cederström, V. Chmill, M. Danielsson, and B. Hasegawa. Evaluation of a photon-counting X-ray imaging system. *IEEE Trans. Nucl. Science*, 48(4):1530–1536, 2001.

[19] M. Åslund, B. Cederström, M. Lundqvist, and M. Danielsson. Scatter rejection in multi-slit digital mammography. *Med. Phys.*, 33:933–940, 2006.

[20] M. Åslund, B. Cederström, M. Lundqvist, and M. Danielsson. Physical characterization of a scanning photon counting digital mammography system based on Si-strip detectors. *Med. Phys.*, 34(6):1918–1925, 2007.

[21] S. Thunberg, L. Adelöw, O. Blom, A. Cöster, J. Egerström, M. Eklund, P. Egnell, T. Francke, U. Jordung, T. Kristoffersson, K. Lindman, L. Lindqvist, D. Marchal, H. Olla, E. Penton, V. Peskov, J. Rantanen, S. Solokov, P. Svedenhag, C. Ullberg, and N. Weber. Dose reduction in mammography with photon counting imaging. In M. J. Yaffe and M. J. Flynn, editors, *Proc. SPIE, Physics of Medical Imaging*, volume 5368, pages 457–465, 2004.

[22] F. Arfelli, V. Bonvicini, A. Bravin, P. Burger, G. Cantatore, E. Castelli, M. Di Michiel, R. Longo, A. Olivo, S. Pani, D. Pontoni, P. Poropat, M. Prest, A. Rashevsky, G. Tromba, A. Vacchi, and N. Zampa. Design and evaluation of AC-coupled, FOXFET-biased, "edge-on" silicon strip detectors for X-ray imaging. *Nucl. Instr. and Meth. A*, 385:311–320, 1997.

[23] A. Bergamaschi, F. Arfelli, D. Dreossi, R. Longo, A. Olivo, S. Pani, L. Rigon, and E. Castelli. Edge on silicon microstrip detectors for medical imaging. *Nucl. Instr. and Meth. A*, 549:199–204, 2005.

[24] C. Avila, J. Lopez, J. C. Sanabria, G. Baldazzi, D. Bollini, M. Gombia, A. E. Cabal, C. Ceballos, A. Diaz Garcia, M. Gambaccini, A. Taibi, A. Sarnelli, A. Tuffanelli, P. Giubellino, A. Marzari-Chiesa, F. Prino, E. Tomassi, P. Grybos, M. Idzik, K. Swientek, P. Wiacek, L. M. Monta no, L. Ramello, and M. Sitta. Contrast cancellation technique applied to digital x-ray imaging using silicon strip detectors. *Med. Phys.*, 32(12):3755–3766, 2005.

[25] S. R. Amendolia, M. G. Bisogni, P. Delogu, M. E. Fantacci, G. Paternoster, V. Rosso, and A. Stefanini. Characterization of a mammographic system based on single photon counting pixel arrays coupled to gaas x-ray detectors. *Med. Phys.*, 36(4):1330–1339, 2009.

[26] G. Blanchot, M. Chmeissani, A. Díaz, F. Díaz, J. Fernández, E. García, J. García, F. Kainberger, M. Lozano, M. Maiorino, R. Martínez, J. P. Montagne, I. Moreno, G. Pellegrini, C. Puigdengoles, M. Sentís, L. Teres, M. Tortajada, and M. Ullán. Dear-mama: A photon counting x-ray imaging project for medical applications. *Nucl. Instr. and Meth. A*, 569(1):136 – 139, 2006.

[27] J. Giersch. Medical quantum x-ray imaging with 2d detectors. *Nucl. Instr. and Meth. A*, 551(1):125 – 138, 2005.

[28] M. V. Yester, G. T. Barnes, and M. A. King. Experimental measurements of the scatter reduction obtained in mammography with a scanning multiple slit assembly. *Med. Phys.*, 8(2):158–162, 1981.

[29] C.D. Bradford, W.W. Peppler, and R.E. Ross. Multitapered x-ray capillary optics for mammography. *Med. Phys.*, 29(6):1097–1108, 2002.

[30] F.R. Sugiro, D. Li, and C.A. MacDonald. Beam collimation with polycapillary x-ray optics for high contrast high resolution monochromatic imaging. *Med. Phys.*, 31(12):3288–3297, 2004.

[31] J.M. Boone, T.R. Fewell, and R.J. Jennings. Molybdenum, rhodium, and tungsten anode spectral models using interpolating polynomials with application to mammography. *Med. Phys.*, 24(12):1863–74, 1997.

[32] M. J. Berger, J. H. Hubbell, S. M. Seltzer, J. S. Coursey, and D. S. Zucker. XCOM: Photon Cross Section Database. http://physics.nist.gov/xcom. National Institute of Standards and Technology, Gaithersburg, MD, 2005.

[33] J.M. Boone. Glandular breast dose for monoenergetic and high-energy x-ray beams: Monte Carlo assessment. *Radiology*, 203:23–37, 1999.

[34] J.W. Motz and M. Danos. Image information content and patient exposure. *Med. Phys.*, 5(1):8–22, 1978.

[35] M.J. Tapiovaara and R.F. Wagner. SNR and DQE analysis of broad spectrum x-ray imaging. *Phys. Med. Biol.*, 30:519–529, 1985.

[36] R.N. Cahn, B. Cederström, M. Danielsson, A. Hall, M. Lundqvist, and D. Nygren. Detective quantum efficiency dependence on x-ray energy weighting in mammography. *Med. Phys.*, 26(12):2680–3, 1999.

[37] R.E. Alvarez and A. Macovski. Energy-selective reconstructions in x-ray computerized tomography. *Phys. Med. Biol.*, 21:733–744, 1976.

[38] L. A. Lehmann, R. E. Alvarez, A. Macovski, W. R. Brody, N. J. Pelc, S. J. Riederer, and A. L. Hall. Generalized image combinations in dual KVP digital radiography. *Med. Phys.*, 8(5):659–667, 1981.

[39] G.E. Pfahler. A roentgen filter and a universal diaphragm and protecting screen. *Trans. Am. Roentgen Ray Soc.*, pages 217–224, 1906.

[40] R.J. Jennings, R.J. Eastgate, M.P Siedband, and D.L. Ergun. Optimal x-ray spectra for screen-film mammography. *Med. Phys.*, 8(5):629–639, 1981.

[41] D. R. Dance, A. Thilander Klang, M. Sandborg, C. L. Skinner, I. A. Castellano Smith, and G. Alm Carlsson. Influence of anode/filter material and tube potential on contrast, signal-to-noise ratio and average absorbed dose in mammography: a Monte Carlo study. *Br. J. Radiol.*, 73(874):1056–67, 2000.

[42] M. Åslund, B. Cederström, M. Lundqvist, and M. Danielsson. Optimization of operating conditions in photon counting multi-slit mammography based on si-strip detectors. *Proc. of SPIE, Medical Imaging 2006*, 6142(79-88), 2006.

[43] E. Burattini, M. Gambaccini, M. Marziani, 0. Rimondi, P. L. lndovina, M. Pocek, G. Simonetti, M. Benassi, C. Tirelli, and R. Passariello. X-ray mammography with synchrotron radiation. *Rev. Sci. Instrum.*, 63(1):638–640, 1992.

[44] R.E. Johnston, D. Washburn, E. Pisano, C. Burns, W.C. Thomlinson, L.D. Chapman, F. Arfelli, N.F. Gmur, Z. Zhong, and D. Sayers. Mammographic phantom studies with synchrotron radiation. *Radiology*, 200:659–663, 1996.

[45] P. Suortti and W. Thomlinson. Medical applications of synchrotron radiation. *Phys. Med. Biol.*, 48(13):R1–R35, 2003.

[46] A. Krol, A. Ikhlef, J.C. Kieffer, D.A. Bassano, C.C. Chamberlain, Z. Jiang, H. Pépin, and S.C. Prasad. Laser-based microfocused x-ray source for mammography: Feasibility study. *Med. Phys.*, 24(5):725–732, 1997.

[47] W. Knüpfer. Feasibility study of a channeling radiation source for applications in the x-ray region. *Nucl. Instr. and Meth. B*, 87:98–103, 1994.

[48] M.A. Piestrup, X. Wu, V.V. Kaplan, S.R. Uglov, J.T. Cremer, D.W. Rule, and R.B. Fiorito. A design of mammography units using a quasimonochromatic x-ray source. *Rev. Sci. Instrum.*, 72(4):2159–2170, 2001.

[49] F. E. Carroll, M. H. Mendenhall, R. H. Traeger, C. Brau, and J. W. Waters. Pulsed Tunable Monochromatic X-Ray Beams from a Compact Source: New Opportunities. *Am. J. Roentgenol.*, 181:1197–1202, 2003.

[50] P. Baldelli, A. Taibi, A. Tuffanelli, M.C. Gilardoni, and M. Gambaccini. A prototype of a quasi-monochromatic system for mammography applications. *Phys. Med. Biol.*, 50:2225–2240, 2005.

[51] R. Lawaczeck, V. Arkadiev, F. Diekmann, and M. Krumrey. Monochromatic x-rays in digital mammography. *Invest. Radiol.*, 40(1):33–39, 2005.

[52] A. Bingölbali and C. A. MacDonald. Curved crystal x-ray optics for monochromatic imaging with a clinical source. *Med. Phys.*, 36(4):1176–1183, 2009.

[53] W. Jark. A simple monochromator based on an alligator lens. *X-Ray Spectrom.*, 33:455–461, 2004.

[54] T. Asaga, S. Chiyasu, S. Mastuda, H. Mastuura, H. Kato, M. Ishida, and T. Komaki. Breast imaging: dual-energy projection radiography with digital radiography. *Radiology*, 164:869–870, 1987.

[55] T. Asaga C. Masuzawa, A. Yoshida, and H. Mastuura. Dual-energy subtraction mammography. *J. Digit. Imaging*, 8(1):70–73, 1995.

[56] A. Taibi, S. Fabbri, P. Baldelli, C. di Maggio, G. Gennaro, M. Marziani, A. Tuffanelli, and M. Gambaccini. Dual-energy imaging in full-field digital mammography: a phantom study. *Phys. Med. Biol.*, 48:1945–1956, 2003.

[57] P.C. Johns and M.J. Yaffe. Theoretical optimization of dual-energy x-ray imaging with application to mammography. *Med. Phys.*, 12:289–296, 1985.

[58] P.C. Johns, D.J. Drost, M.J. Yaffe, and A. Fenster. Dual-energy mammography: initial experimental results. *Med. Phys.*, 12:297–304, 1985.

[59] K. Bliznakova, Z. Kolitsi, and N. Pallikarakis. Dual-energy mammography: simulation studies. *Phys. Med. Biol.*, 51(18):4497–4515, 2006.

[60] J.M. Boone, G.S. Shaber, and M. Tcotzky. Dual energy mammography: a detector analysis. *Med. Phys.*, 17:665–675, 1990.

[61] D. P. Chakraborty and G. T. Barnes. An energy sensitive cassette for dual-energy mammography. *Med. Phys.*, 16:7–13, 1989.

[62] M. R. Lemacks, S. C. Kappadath, C. C. Shaw, X. Liu, and G. J. Whitman. A dual-energy subtraction technique for microcalcification imaging in digital mammography—a signal-to-noise analysis. *Med. Phys.*, 29(8):1739–1751, 2002.

[63] S. C. Kappadath and C. C. Shaw. Qunatitative evaluation of dual-energy digital mammography for calcification imaging. *Phys. Med. Biol.*, 53(19):5421–5443, 2008.

[64] D. S. Brettle and A. R. Cowen. Dual-energy digital mammography utilizing stimulated phosphor computed radiography. *Phys. Med. Biol.*, 39(11):1989–2004, 1994.

[65] N. Weidner, J.P. Semple, W.R. Welch, and J. Folkman. Tumour angiogenesis and metastasis: correlation in invasive breast carcinoma. *N. Engl. J. Med.*, 324(1):1–8, 1991.

[66] J.M. Lewin, P.K. Isaacs, V. Vance, and F.J. Larke. Dual-energy contrast-enhanced digital subtraction mammography: Feasibility. *Radiology*, 229:261–268, 2003.

[67] P. Baldelli, A. Bravin, C. Di Maggio, G. Gennaro, A. Sarnelli, A. Taibi, and M. Gambaccini. Evaluation of the minimum iodine concentration for contrast-enhanced subtraction mammography. *Phys. Med. Biol.*, 51(17):4233–51, 2006.

[68] H. Bornefalk, J. M. Lewin, M. Danielsson, and M. Lundqvist. Single-shot dual-energy subtraction mammography with electronic spectrum splitting: Feasibility. *Eur. J. Radiol.*, 60:275–278, 2006.

[69] H. Bornefalk, M. Hemmendorff, and T. Hjärn. Contrast-enhanced dual-energy mammography using a scanned multislit system: evaluation of a differential beam filtering technique. *J. Electron. Imaging*, 16(2), 2007.

[70] M. Skarpathiotakis, M. J. Yaffe, A. K. Bloomquist, D. Rico, S. Muller, A. Rick, and F. Jeunehomme. Development of contrast digital mammography. *Med. Phys.*, 29(10):2419–2426, 2002.

[71] F. Diekmann, S. Diekmann, M. Taupitz, U. Bick, K.-J. Winzer, C. Hüttner, S. Muller, F. Jeunehomme, and B. Hamm. Use of iodine-based contrast media in digital full-field mammography - initial experience. *Fortschr. Röntgenstr.*, 175:342–345, 2003.

[72] S. Feuerlein, E. Roessl, R. Proksa, G. Martens, O. Klass, M. Jeltsch, V. Rasche, H. J. Brambs, M. H. K. Hoffmann, and J. P. Schlomka. Multienergy photon-counting k-edge imaging: Potential for improved luminal depiction in vascular imaging. *Radiology*, 249:1010–1016, 2008.

[73] J. P. Schlomka, E. Roessl, R. Dorscheid, S. Dill, G. Martens, T. Istel, C. Bäumer, C. Herrmann, R. Steadman, G. Zeitler, A. Livne, and R. Proksa. Experimental feasibility of multi-energy photon-counting k-edge imaging in pre-clinical computed tomography. *Phys. Med. Biol.*, 53:4031–4047, 2008.

[74] B. Cederström. *A multi-prism lens for hard x-rays.* PhD thesis, Royal Institute of Technology (KTH), Stockholm, 2002.

[75] The HighReX Project (High Resolution X-ray imaging). online: http://www.highrex.eu.

[76] M. Lundqvist. *Silicon strip detectors for scanned multi-slit x-ray imaging.* PhD thesis, Royal Institute of Technology (KTH), Stockholm, 2003.

[77] M. Åslund. *Digital Mammography with a Photon Counting Detector in a Scanned Multislit Geometry.* PhD thesis, Royal Institute of Technology (KTH), Stockholm, 2007.

[78] H. Bornefalk. *Computer-aided detection and novel mammography imaging techniques.* PhD thesis, Royal Institute of Technology (KTH), Stockholm, 2006.

[79] B. X. Yang. Fresnel and refractive lenses for x-rays. *Nucl. Instr. and Meth. A*, 1993.

[80] A. G. Michette. No X-ray lens. *Nature*, 353:510, 1991.

[81] A. Snigirev, V. Kohn, I. Snigireva, and B. Lengeler. A compound refractive lens for focusing high-energy X-rays. *Nature*, 384:49–51, 1996.

[82] B. Lengeler, J. Tümmler, A. Snigirev, I. Snigireva, and C. Raven. Transmission and gain of singly and doubly focusing refractive x-ray lenses. *J. Appl. Phys.*, 84(11):5855–5861, 1998.

[83] B. Cederström, R. Cahn, M. Danielsson, M. Lundqvist, and D. Nygren. Focusing hard x-rays with old LP's. *Nature*, 404:951, 2000.

[84] B. Cederström, M. Lundqvist, and C. Ribbing. Multi-prism x-ray lens. *Appl. Phys. Lett.*, 81(8):1399–1401, 2002.

[85] S. Suehiro, M. Miyaji, and H. Hayashi. Refractive lens for x-ray focus. *Nature*, 352:385–386, 1991.

[86] V. Aristov, M. Grigoriev, S. Kuznetsov, L. Shabelnikov, V. Yunkin, T. Weitkamp, C. Rau, I. Snigireva, A. Snigirev, M. Hoffmann, and E. Voges. X-ray refractive planar lens with minimized absorption. *Appl. Phys. Lett.*, 77 (24):4058–4060, 2000.

[87] M. A. Piestrup, J. T. Cremer, H. R. Beguiristain, C. K. Gary, and R. H. Pantell. Two-dimensional x-ray focusing from compound lenses made of plastic. *Rev. Sci. Instrum.*, 71(12):4375–4379, 2000.

[88] B. Cederström, C. Ribbing, and M. Lundqvist. Generalized prism-array lenses for hard x-rays. *J. Synchrotron Rad.*, 12:340–344, 2005.

[89] W. Jark, F. Pérennès, M. Matteucci, L. Mancini, L. Montanari, L. Rigon, G. Tromba, A. Somogyi, R. Tucoulou, and S. Bohic. Focusing x-rays with simple arrays of prism-like structures. *J. Synchrotron Rad.*, 11:248–253, 2004.

[90] B. Cederström, C. Ribbing, and M. Lundqvist. Saw-tooth refractive x-ray optics with sub-micron resolution. In D. C. Mancini, editor, *Proc. SPIE, Design and Microfabrication of Novel X-Ray Optics*, volume 4783, pages 37–48, 2002.

[91] E. M. Dufresne, D. A. Arms, R. Clarke, N. R. Pereira, S. B. Dierker, and D. Foster. Lithium metal for x-ray refractive optics. *Appl. Phys. Lett.*, 79 (25):4085–4087, 2001.

[92] C. Ribbing, B. Cederström, and M. Lundqvist. Microfabrication of saw-tooth refractive x-ray lenses in low-Z materials. *J. Micromech. Microeng.*, 13:714–720, 2003.

[93] K. Evans-Lutterodt, J. Ablett, A. Stein, C. Kao, D. Tennant, F. Klemens, A. Taylor, C. Jacobsen, P. Gammel, H. Huggins, G. Bogart, S. Ustin, and L. Ocola. Single-element elliptical hard x-ray micro-optics. *Opt. Express*, 11 (8):919–926, 2003.

[94] B. Nöhammer, J. Hoszowska, A. K. Freund, and C. David. Diamond planar refractive lenses for third- and fourth-generation X-ray sources. *J. Synchrotron Rad.*, 10(2):168–171, 2003.

[95] V. Nazmov, L. Shabel'nikov, F. J. Pantenburg, J. Mohr, E. Reznikova, A. Snigirev, I. Snigireva, S. Kouznetsov, and M. DiMichiel. Kinoform X-ray lens creation in polymer materials by deep X-ray lithography. *Nucl. Instr. and Meth. B*, 217(3):409 – 416, 2004.

[96] F. Pérennès, M. Matteucci, W. Jark, and B. Marmiroli. Fabrication of refractive X-ray focusing lenses by deep X-ray lithography. *Microelectronic Engineering*, 78-79:79 – 87, 2005.

[97] B. Niemann, D. Rudolph, and G. Schmahl. Soft x-ray imaging zone plates with large zone numbers for microscopic and spectroscopic applications. *Opt. Commun.*, 12(2):160 – 163, 1974.

[98] U. Vogt, M. Wieland, T. Wilhein, M. Beck, and H. Stiel. Design and application of a zone plate monochromator for laboratory soft x-ray sources. *Rev. Sci. Instrum.*, 72(1):53–57, 2001.

[99] E. Fredenberg, B. Cederström, C. Ribbing, and M. Danielsson. Prism-array lenses for energy filtering in medical x-ray imaging. In M. J. Flynn and J. Hsieh, editors, *Proc. SPIE, Physics of Medical Imaging*, volume 6510, 2007.

[100] V. V. Aristov, V. V. Starkov, L. G. Shabel'nikov, S. M. Kuznetsov, A. P. Ushakova, M. V. Grigoriev, and V. M. Tseitlin. Short-focus silicon parabolic lenses for hard X-rays. *Opt. Commun.*, 161(4-6):203 – 208, 1999.

[101] R Fahrig and M J Yaffe. Optimization of spectral shape in digital mammography: dependence on anode material, breast thickness, and lesion type. *Med Phys*, 21(9):1473–81, 1994.

[102] X. Wu and H. Liu. Clinical implementation of x-ray phase contrast imaging: theoretical foundations and design considerations. *Med. Phys.*, 30:2169–2179, 2003.

[103] T. Tuohimaa, J. Ewald, M. Schlie, J. M. Fernández-Varea, H. M. Hertz, and U. Vogt. A microfocus x-ray source based on a nonmetal liquid-jet anode. *Appl. Phys. Lett.*, 92(23):233509, 2008.

[104] P. C. Johns and M. J. Yaffe. X-ray characterisation of normal and neoplastic breast tissues. *Phys. Med. Biol.*, 32(6):675–695, 1987.

[105] S. Richard and J. H. Siewerdsen. Optimization of dual-energy imaging systems using generalized NEQ and imaging task. *Med. Phys.*, 34(1):127–139, 2007.

[106] S. Richard and J. H. Siewerdsen. Comparison of model and human observer performance for detection and discrimination tasks using dual-energy x-ray images. *Med. Phys.*, 35:5043–5053, 2008.

[107] I. A. Cunningham. *Handbook of Medical Imaging*, volume 1. Physics and Psychophysics, chapter 2. Applied Linear-Systems Theory. SPIE Press, Bellingham, USA, 2000.

[108] A. Teifke, F. Schweden, H. Cagil, H.U. Kauczor, W. Mohr, and M. Thelen. Spiral-Computertomographie der Mamma. *Rofo*, 161(6):495–500, 1994.

[109] F.O. Bochud, C.K. Abbey, and M.P. Eckstein. Statistical texture synthesis of mammographic images with clustered lumpy backgrounds. *Opt. Express*, 4(1):33–43, 1999.

[110] D. Reintgen, C. Berman, C. Cox, P. Baekey, S. Nicosia, H. Greenberg, C. Bush, G. H. Lyman, and R. A. Clark. The anatomy of missed breast cancers. *Surgical Oncology*, 2(1):65 – 75, 1993.

[111] S. Richard and J. H. Siewerdsen. Cascaded systems analysis of noise reduction algorithms in dual-energy imaging. *Med. Phys.*, 35(2):586–601, 2008.

[112] M. Båth, M. Håkansson, and L. G. Månsson. Determination of the two-dimensional detective quantum efficiency of a computed radiography system. *Med. Phys.*, 30(12):3172–3182, 2003.

[113] J.J. Heine and R.P. Velthuizen. Spectral analysis of full field digital mammography data. *Med. Phys.*, 29(5):647–661, 2002.

[114] S. Richard, J. H. Siewerdsen, D. A. Jaffray, D. J. Moseley, and B. Bakhtiar. Generalized DQE analysis of radiographic and dual-energy imaging using flat-panel detectors. *Med. Phys.*, 32(5):1397–1413, 2005.

[115] M. Båth, M. Håkansson, S. Börjesson, C. Hoeschen, O. Tischenko, S. Kheddache, J. Vikgren, and L. G. Månsson. Nodule detection in digital chest radiography: effect of anatomical noise. *Radiat. Prot. Dosimetry*, 114(1-3): 109–113, 2005.

[116] E. Fredenberg, B. Cederström, M. Lundqvist, C. Ribbing, M. Åslund, F. Diekmann, R. Nishikawa, and M. Danielsson. Contrast-enhanced dual-energy subtraction imaging using electronic spectrum-splitting and multi-prism x-ray lenses. In J. Hsieh and E. Samei, editors, *Proc. SPIE, Physics of Medical Imaging*, volume 6913, 2008.

[117] A.-K. Carton, S. C. Gavenonis, J. A. Currivan, E. F. Conant, M. D. Schnall, and A. D. A. Maidment. Dual-energy contrast-enhanced digital breast tomosynthesis – a feasibility study. *Br. J. Radiol.*, page 80279516, 2009.

[118] E. Fredenberg, M. Lundqvist, M. Åslund, M. Hemmendorff, B. Cederström, and M. Danielsson. A photon-counting detector for dual-energy breast tomosynthesis. In J. Hsieh and E. Samei, editors, *Proc. SPIE, Physics of Medical Imaging*, volume 7258, 2009.